SANDIA REPORT
SAND2022-1479
Printed February 2022

Sandia National Laboratories

Verification and Validation Activities for the Multi-Fidelity Toolkit

Blake W. Lance, Aaron M. Krueger, Brian A. Freno, Ross M. Wagnild

Prepared by
Sandia National Laboratories
Albuquerque, New Mexico 87185
Livermore, California 94550

Issued by Sandia National Laboratories, operated for the United States Department of Energy by National Technology & Engineering Solutions of Sandia, LLC.

Available to DOE and DOE contractors from

U.S. Department of Energy
Office of Scientific and Technical Information
P.O. Box 62
Oak Ridge, TN 37831

Telephone: (865) 576-8401
Facsimile: (865) 576-5728
E-Mail: reports@osti.gov
Online ordering: http://www.osti.gov/scitech

Available to the public from

U.S. Department of Commerce
National Technical Information Service
5301 Shawnee Road
Alexandria, VA 22312

Telephone: (800) 553-6847
Facsimile: (703) 605-6900
E-Mail: orders@ntis.gov
Online order: https://classic.ntis.gov/help/order-methods

ABSTRACT

The Multi-Fidelity Toolkit (MFTK) is a simulation tool being developed at Sandia National Laboratories for aerodynamic predictions of compressible flows over a range of physics fidelities and computational speeds. These models include the Reynolds-Averaged Navier–Stokes (RANS) equations, the Euler equations, and modified Newtonian aerodynamics (MNA) equations, and they can be invoked independently or coupled with hierarchical Kriging to interpolate between high-fidelity simulations using lower-fidelity data. However, as with any new simulation capability, verification and validation are necessary to gather credibility evidence. This work describes formal code- and solution-verification activities as well as model validation with uncertainty considerations. Code verification is performed on the MNA model by comparing with an analytical solution for flat-plate and inclined-plate geometries. Solution-verification activities include grid-refinement studies of HIFiRE-1 wind tunnel measurements, which are used for validation, for all model fidelities. A thorough treatment of the validation comparison with prediction error and validation uncertainty is also presented.

ACKNOWLEDGMENT

The authors wish to thank Greg Weirs, Derek Dinzl, and Jaideep Ray for their insights into the HIFiRE-1 experiments as well as previous simulations performed at Sandia National Laboratories. The authors also wish to thank Matthew Bopp, Brian Carnes, and Bryan Morreale for their help in setting up the code-verification cases.

CONTENTS

1. Introduction **9**

2. Code Verification **11**
2.1. Code Verification with Analytical Solutions . . . 11
2.2. Verification Cases . . . 12
2.2.1. Case 1: Flat Plate . . . 12
2.2.2. Case 2: Inclined Plate . . . 14
2.2.3. Coding Error Identified . . . 16
2.3. Future Work . . . 16

3. Solution Verification **17**
3.1. GCI Equations . . . 17
3.2. Solution Verification Assessment . . . 18
3.2.1. MNA+FPBL with 0° Angle of Attack . . . 19
3.2.2. Euler+MEIT with 0° Angle of Attack . . . 22
3.2.3. RANS with 0° Angle of Attack . . . 23
3.3. Future Work . . . 25

4. Validation **26**
4.1. Model Validation Theory . . . 26
4.2. HIFiRE-1 Wind Tunnel Tests . . . 27
4.3. Validation Results . . . 28
4.3.1. Surface Pressure Comparisons . . . 30
4.3.2. Surface Heat Flux Comparisons . . . 34
4.3.3. Future Work . . . 40

5. Conclusions **41**

References **43**

Appendices **46**

A. Derivation of Modified Newtonian Aerodynamics **46**
A.1. Assumed Inputs . . . 46
A.2. Newtonian Theory . . . 46
A.3. MNA Model . . . 47
A.4. Flat Plate Boundary Layer Model . . . 48
A.4.1. Shear Stress . . . 49
A.4.2. Heat Flux . . . 51

LIST OF FIGURES

Figure 2-1. Computational domain for the flat-plate case (side view). 12
Figure 2-2. Coarsest mesh for the flat-plate case (top view). 13
Figure 2-3. Computational domain for the inclined-plate case. 14
Figure 2-4. Coarsest Mesh for the inclined-plate case. 15

Figure 3-1. MNA+FPBL coarse mesh example in nose-cone region. 17
Figure 3-2. Euler+MEIT and RANS coarse mesh examples in nose-cone region. 18
Figure 3-3. The HIFiRE-1 wind tunnel test geometry that shows the fore-cone on the left, the cylindrical section in the center, and the flare on the right, from [1]. The text states that the final nosetip was changed from sharp to a radius of 2.5 mm and the flare angle was changed from 37° to 33°. 19
Figure 3-4. GCI calculation for laminar case with 0° angle of attack. 20
Figure 3-5. GCI calculation for turbulent (Van Driest) case with 0° angle of attack. . . . 21
Figure 3-6. GCI calculation for turbulent (MEIT) case with 0° angle of attack. 22
Figure 3-7. GCI calculation for turbulent (SA) case with 0° angle of attack. 23
Figure 3-8. GCI Calculation for turbulent (SST) case with 0° angle of attack. 24

Figure 4-1. HIFiRE-1 wind tunnel simulation Mach number predictions for RANS-SA and RANS-SST models. 29
Figure 4-2. HIFiRE-1 wind tunnel test pressure data and predictions. 31
Figure 4-3. HIFiRE-1 pressure prediction error with uncertainty. 32
Figure 4-4. HIFiRE-1 pressure prediction error magnitude integrated over data with uncertainty. 33
Figure 4-5. HIFiRE-1 pressure prediction error magnitude separated by section with uncertainty. 35
Figure 4-6. HIFiRE-1 wind tunnel test heat flux data and predictions. 36
Figure 4-7. HIFiRE-1 heat flux prediction error with uncertainty. 37
Figure 4-8. HIFiRE-1 heat flux prediction error magnitude integrated over data with uncertainty. 38
Figure 4-9. HIFiRE-1 heat flux prediction error magnitude by section with uncertainty. 39

LIST OF TABLES

Table 2-1. Code-verification results for the flat-plate case. 13
Table 2-2. Code verification results for the inclined-plate case 15

Table A-1. Table of values used in code-verification analysis. 46

1. INTRODUCTION

The Multi-Fidelity Toolkit (MFTK) is a suite of tools being developed at Sandia National Laboratories to improve the response time for aerothermodynamic queries for hypersonic flight vehicles. The toolkit comprises three levels of aerothermodynamic physics fidelity and a series of file- and data-handling scripts: an input-file generator, a sample-point dispatcher, a data-gathering code, and a multi-fidelity interpolation code. The aerothermodynamic evaluation fidelity levels are being developed in the Sandia Parallel Aerodynamics and Reentry Code (SPARC) and consist of a modified Newtonian aerodynamics (MNA) solver, an Euler solver, and a Reynolds-Averaged Navier–Stokes (RANS) solver. The low- and medium-fidelity models do not have the ability to compute viscous effects such as heat flux; therefore, both transfer data to different correlation-based models. The multi-fidelity interpolation code uses a hierarchical Kriging method [2] to perform sample evaluations over a parameter space by using trends from lower-fidelity predictions and anchoring to high-fidelity predictions, such as those from a RANS solver. This allows for more accurate predictions to be computed over a large parameter space at a reduced cost, compared to running a RANS solver only. With the multi-fidelity interpolation method, the focus of the lower-fidelity methods is on minimizing the error in the trend of aerothermodynamic data rather than the absolute error of each model. However, achieving the expected order of accuracy is necessary to ensure the lower-fidelity models have been correctly implemented.

To assess the credibility of predictions using MFTK, verification and validation activities are performed to ensure the correct implementation and appropriate use of the models. Validation assesses how well the implemented models represent the relevant physical phenomena. This is typically done by comparing simulation predictions with experimental data to assess the modeling error and ultimately the bounds of validity for a defined application space. By contrast, verification is, according to the American Society of Mechanical Engineers (ASME) Standard for Verification and Validation in Computational Solid Mechanics [3], "the process of determining that a computational model accurately represents the underlying model and its solution." Verification is further broken up into code verification and solution verification [4–6]. Code verification focuses on the correct implementation of the mathematical model, whereas solution verification focuses on estimating the numerical error for a particular solution.

Previous work on the underlying models includes code verification of the Euler equations [7] and code and solution verification of laminar equations [8]. To continue this effort, this paper focuses on code verification of the MNA model and solution verification of all the models in MFTK. When solving the underlying equations numerically, the geometry is discretized over the surface of the body. One consequence of discretizing the geometry is

that the solution incurs a truncation error, which introduces a discretization error into the solution. By refining the mesh for a problem with a known solution and measuring the corresponding decrease in the L^∞-norm of the discretization error, we compute an observed order of accuracy and compare it to the theoretical order of accuracy. When the comparison is sufficiently close, the likelihood of coding errors existing within the code is greatly reduced.

For solution verification, the exact solution is unknown. Therefore, we estimate the discretization error using the grid convergence index (GCI) metric [9]. GCI uses the difference between the Richardson extrapolated solution and the solution on the finest mesh as an approximation of the discretization error. To account for uncertainty within the calculation, the GCI metric applies a factor-of-safety multiplier to the estimated discretization error to account for errors not captured in the Richardson extrapolation calculation. The GCI metric is then applied as a bound on both sides of the solution on the finest mesh. Additional solution-verification methods exist [10–12], but these methods can be unnecessarily complex for simple problems.

Model validation is defined by both the American Institute of Aeronautics and Astronautics (AIAA) "Guide for Verification and Validation of Computational Fluid Dynamics Simulations" and the ASME "Standard for Verification and Validation in Computational Fluid Dynamics and Heat Transfer" as, "the process of determining the degree to which a model is an accurate representation of the real world from the perspective of the intended uses of the model." [13, 14].

The scope of this work does not include the multi-fidelity interpolation aspect of MFTK because it is applied to a single parameter set for the validation case instead of a parameter exploration. Instead, predictions are made at each fidelity level independently to assess predictive accuracy, with the understanding that lower-fidelity models are expected to have lower accuracy. The low-fidelity MNA model may occasionally be executed independently, but its main purpose is to predict trend information with many runs across a parameter sweep. The mid-fidelity Euler solver may be run independently for quick-turnaround simulations or potentially in a Monte Carlo-style uncertainty quantification (UQ) analysis, so predictive accuracy is more desirable and expected here.

2. CODE VERIFICATION

Code verification is the first credibility activity to be completed for MFTK. This is done to ensure that coding errors are removed before impacting solution-verification or validation activities. The code-verification activities for this report focus on verifying the MNA model within MFTK. The MNA model is the inviscid component of the low-fidelity model within MFTK. In conjunction with a viscous component, such as flat-plate boundary layer (FPBL) model, MFTK computes surface quantities for hypersonic flow calculations. MNA falls under the umbrella of local surface inclination methods. It is an improvement on Newtonian theory by accounting for the freestream Mach number when computing the coefficient of pressure [15]. Newtonian and MNA methods solve for the pressure coefficients, which in turn, allow for solving the surface pressure distribution. This method assumes parallel streamlines directed towards a surface. In the presence of a surface, such as an inclined plane, the fluid creates a pressure on the surface. While this model does not perform well for low-Mach flow, it has the potential to accurately model hypersonic flow when a thin hypersonic shock layer exists and most of the momentum from the fluid is transferred to redirecting the fluid. Additionally, the MNA model within MFTK also includes surface calculations of velocity, temperature, and streamline length based on tangential velocity vectors and streamline marching. Using the MNA+FPBL model, these streamlines enable one to compute the shear stress and heat flux using a one-dimensional viscous model [16]. To complete an in-depth code-verification analysis, a proper understanding of the equations (shown in Appendix A) and cases with known solutions are required.

2.1. Code Verification with Analytical Solutions

Typically, code-verification activities involve verifying differential or integral equations that introduce discretization error into the solution. Because of the simplicity of the MNA model, initial code-verification test cases do not introduce discretization error. Therefore, the relative difference between an exact solution from a separate code and the computed solution from MFTK should be approximately round-off error, such that, if the L^∞-norm

$$\varepsilon_\infty = \max_i \left| \frac{\mathrm{QoI}_{i_{\mathrm{Exact}}} - \mathrm{QoI}_{i_{\mathrm{MFTK}}}}{\mathrm{QoI}_{i_{\mathrm{Exact}}}} \right|, \tag{2.1}$$

where QoI is the quantity of interest, is less than 10^{-12}, the test passes.

2.2. Verification Cases

For this analysis, two code-verification cases are studied to identify implementation (also know as constant errors) and meshing errors. Case 1 is a flat-plate case and Case 2 is an inclined-plate case. The flat-plate case is almost identical to inclined-plate case except that the mesh for the inclined-plate case can introduce mesh tolerance errors when inclining the plate. Instead, the flat-plate case inclines the freestream velocity to induce the pressure field since the precision of the freestream velocity is less prone to errors. For both test cases, the following MNA model QoIs are tested: C_p, P_e, $\mathbf{V}_e$, M_e, T_e, ρ_e, $\mathbf{n}_v$, and L. We note that Case 1 and Case 2 do not identify geometry discretization errors, which require order-of-accuracy testing and is left for future work.

2.2.1. Case 1: Flat Plate

The flat-plate case models flow over a flat plate, where the angle of attack is $-7°$. The computational domain of the flat-plate case is a 1.0 m by 1.0 m square on the XZ-plane, which is shown in Figure 2-1. Since the mesh perfectly represents the geometry and the mesh is aligned with the streamlines, which is shown in Figure 2-2, this case uses an analytical solution to test the correct implementation. This case provides the most simplistic MNA model test case to ensure all variables computed by MFTK match the exact solution.

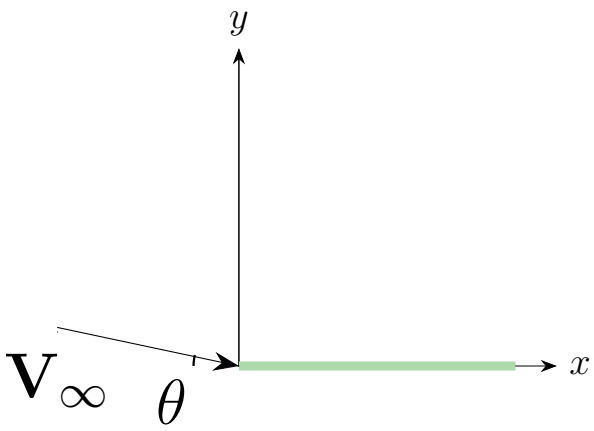

Figure 2-1. Computational domain for the flat-plate case (side view).

The exact solution uses input from Table A-1 in conjunction with Equations (A.11) through (A.18) and the velocity specified above. Using Equation (2.1), the relative error is computed. The results of the code-verification analysis are shown in Table 2-1.

All of the errors in the MNA variables are below 10^{-13} and clearly below the test criteria of 10^{-12}, which means the MNA model equations do not have constant errors when the

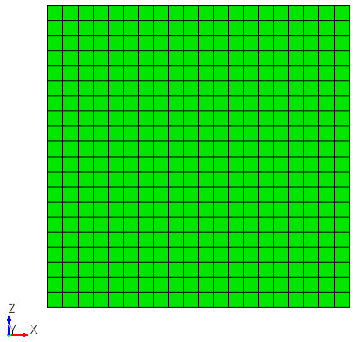

Figure 2-2. Coarsest mesh for the flat-plate case (top view).

Table 2-1. Code-verification results for the flat-plate case.

Variable	Mesh 1 Error	Mesh 2 Error	Mesh 3 Error	Mesh 4 Error
n_x	0.00	0.00	0.00	0.00
n_y	0.00	0.00	0.00	0.00
C_p $[\times 10^{-14}]$	9.67	9.67	9.67	9.67
P $[\times 10^{-14}]$	3.18	3.18	3.18	3.18
u $[\times 10^{-14}]$	5.31	5.31	5.31	5.31
v	0.00	0.00	0.00	0.00
M $[\times 10^{-15}]$	8.14	8.14	8.14	8.14
T $[\times 10^{-15}]$	2.06	2.06	2.06	2.06
ρ $[\times 10^{-14}]$	5.97	5.97	5.97	5.97
Dist $[\times 10^{-16}]$	2.18	2.07	2.07	1.71

staggered mesh is aligned, which simplifies the streamline calculation. If an implementation error were present, the relative error would be much higher than 10^{-13}, making this verification test quite sensitive to constant errors. One note in completing this verification testing is that precision tolerances are much more important for these tests than realistic problems. This makes setting up the test cases difficult since hidden or rarely used settings can cause issues to the results. We also note that the error in the streamline distance is increasing with mesh refinement. Increasing error is to be expected since round-off error increases with the number of calculations being performed.

2.2.2. Case 2: Inclined Plate

The inclined-plate case is identical to the flat-plate case, but the implementation is slightly different. For this case, the velocity is along the x-axis and the plate is inclined by 7°, as shown in Figure 2-3. Since the mesh perfectly represents the geometry and the mesh is aligned with the streamlines, this case uses an analytical solution to test the correct implementation. This case provides the second most simplistic MNA model test case to ensure all variables computed by MFTK match the exact solution.

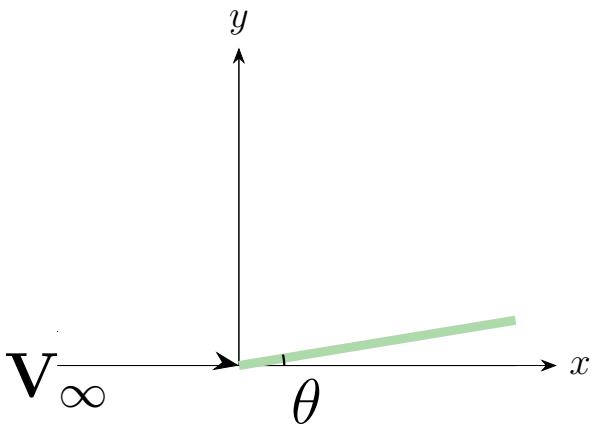

Figure 2-3. Computational domain for the inclined-plate case.

The exact solution uses input from Table A-1 in conjunction with Equations (A.11) through (A.18) and the velocity specified in Section 2.2.2. Using Equation (2.1), the relative error is computed, and the results are shown in Table 2-2.

All of the errors in the MNA variables are at most $\sim 10^{-13}$ and clearly below the test criteria of 10^{-12}, which means the MNA model equations do not have constant errors when the staggered mesh is aligned, which simplifies the streamline calculation. One note on this particular problem is that initial results were impacted by the precision of the mesh. This

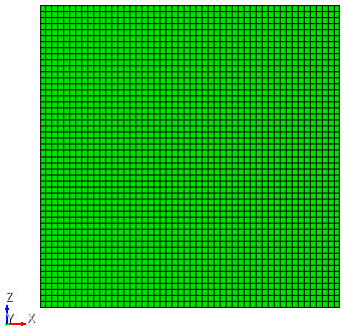

Figure 2-4. Coarsest Mesh for the inclined-plate case.

Table 2-2. Code verification results for the inclined-plate case

Variable	Mesh 1 Error	Mesh 2 Error	Mesh 3 Error	Mesh 4 Error
n_x $[\times 10^{-13}]$	4.76	4.36	4.35	4.08
n_y $[\times 10^{-14}]$	2.36	2.29	2.26	2.24
C_p $[\times 10^{-13}]$	2.72	2.72	2.72	0.97
P $[\times 10^{-13}]$	1.48	0.84	0.32	0.32
u $[\times 10^{-13}]$	1.55	1.54	1.54	1.54
v $[\times 10^{-13}]$	1.38	0.91	0.47	0.19
M $[\times 10^{-15}]$	8.14	8.14	8.14	8.14
T $[\times 10^{-15}]$	2.06	2.06	2.06	2.06
ρ $[\times 10^{-14}]$	5.97	5.97	5.97	5.97
Dist $[\times 10^{-14}]$	9.51	4.42	1.63	0.92

problem requires the maximum precision available from the meshing software to ensure mesh precision does not impact the exact verification results.

2.2.3. Coding Error Identified

During the development of Cases 1 and 2, a coding error in how the stagnation point is computed at the edge of a face was identified and corrected. Partial geometry simulations are undertaken to reduce the computational cost of the simulation by utilizing symmetry within the solution. Since partial geometries would have the stagnation point located at the edge of a face, this coding error would have impacted all partial geometry simulations. This finding highlights the importance of completing code verification.

2.3. Future Work

For future work, an additional test case should also be completed to ensure the MNA model can pass an order-of-accuracy test. One proposed test case would be simulating flow over a blunt-nose cone. This curved geometry would introduce geometry discretization error as well as discretization error from the streamline distance calculation because of the use of an unstructured grid. Additionally, code verification of the FPBL model should be completed for all three test cases. Lastly, code verification should be applied to the momentum/energy integral technique (MEIT) since there is currently no code verification for the implementation within MFTK. Once all these tests have been successfully implemented, these code-verification tests should be automated to ensure MFTK continues to pass these tests with ongoing development.

3. SOLUTION VERIFICATION

Once code-verification activities are complete, solution-verification activities can start. Solution-verification activities assesses how well discrete equations can approximate the converged solution. This is crucial to complete before validation activities start because the numerical uncertainty can impact the validation assessment. Since the different models in MFTK (MNA, Euler, and RANS) use discrete equations to represent the model, an assessment of the numerical uncertainty needs to be completed for each validation case. For an initial assessment of numerical uncertainty, we will use the GCI metric.

3.1. GCI Equations

The grid convergence index (GCI) is the most simple and popular method to assess numerical uncertainty. GCI requires solutions on at least three mesh sets (f_1, f_2, and f_3) to compute the observed order of accuracy. The base case developed for the validation study produced a solution on the medium mesh. For this study, a coarser and finer mesh were developed with a refinement (and coarsening) factor of two ($r = 2$) to generate the additional solutions required. Since the MNA+FPBL model is a panel method, whereas Euler+MEIT and both RANS models are control-volume methods, two separate mesh triplets were generated. Figure 3-1 shows the coarsest 3D surface mesh used for the MNA+FPBL model, whereas Figure 3-2 shows the coarsest 2D axisymmetric volume mesh used for the Euler+MEIT and both RANS models. For both meshes, the only significant mesh refinement is near the nose-cone region since large gradients are expected in this region. Each figure focuses on the mesh resolution details in the nose-cone region. The medium and fine cell sizes can resolve length scales approximately two- and four-times smaller than the coarse cell sizes, respectively.

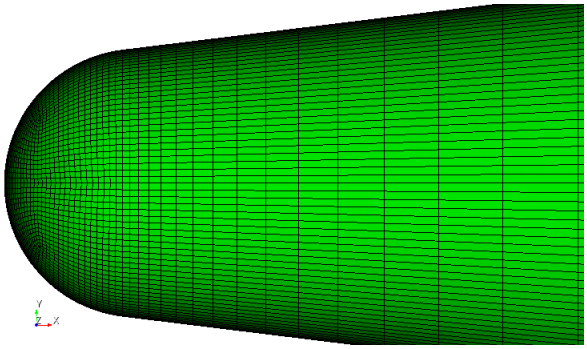

Figure 3-1. MNA+FPBL coarse mesh example in nose-cone region.

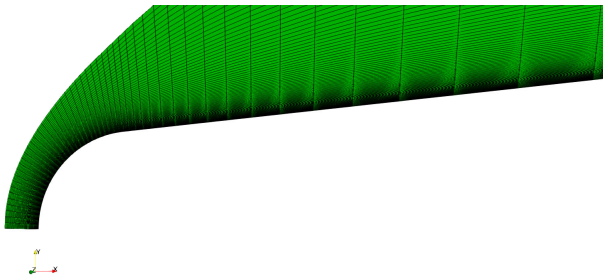

Figure 3-2. Euler+MEIT and RANS coarse mesh examples in nose-cone region.

This provides enough information to compute the observed order of accuracy, p_{obs}, which is

$$p_{\text{obs}} = \frac{\ln\left(\frac{f_3 - f_2}{f_2 - f_1}\right)}{\ln r}. \tag{3.1}$$

Once we compute the p_{obs}, a factor of safety, F_s, is chosen. This factor of safety turns the discretization error estimate into a 95% confidence interval. Based on [5], when the difference between p_{obs} and the theoretical order of accuracy, p_{th}, is smaller than 10%, $F_s = 1.25$. For all other cases, $F_s = 3.0$. While multiplying the estimated discretization error significantly inflates the reported error, being close to or outside the asymptotic range can negatively impact the quality of the Richardson extrapolation. Additionally, when p_{obs} is positive, but larger in magnitude than p_{th}, it is conservative to use p_{th} in the GCI metric, which will be seen in the order-of-accuracy plots below as a ceiling. When p_{obs} is smaller in magnitude than p_{th}, it is conservative to use p_{obs} in the GCI metric. For the case when p_{obs} is positive, but less than 0.5, the order of accuracy is set to 0.5, which will be seen in the order-of-accuracy plots below as a floor. For the case when p_{obs} is negative, this suggests that the simulation is non-convergent and numerical uncertainty cannot be estimated. Now that F_s and p are known, the GCI metric is computed using

$$\text{GCI} = F_s \frac{|f_3 - f_2|}{(r^p - 1)} \tag{3.2}$$

3.2. Solution Verification Assessment

For the solution verification assessment, there are a variety of fidelities and viscous models assessed to match the validation assessment of the HIFiRE-1 wind tunnel test in Chapter 4. To assess the numerical uncertainty for each simulation case, the GCI is computed along the downstream flow. The HIFiRE-1 geometry, shown in Figure 3-3, is used for all simulation cases. The model fidelities assessed are MNA+FPBL, Euler+MEIT, and Reynold-averaged Navier–Stokes (RANS) for the 0° angle of attack case. Since the validation assessment is performed on the pressure (P) and wall heat flux (q_w), the solution-verification assessment needs to quantify the numerical uncertainty for those QoIs. In addition to the normalized GCI values, we report simulation results for each level of

refinement to quickly assess the mesh sensitivity. Lastly, we also report the observed order of accuracy to show how well the numerical method is performing. For all simulation results, except for the heat flux results from the MNA+FPBL model, the theoretical order of accuracy is assumed to be two, due to the linear approximation of the angle. For the heat-flux results in the MNA+FPBL model, the theoretical order of accuracy is assumed to be one, due to the sub-linear approximation of the streamline distance. To ensure consistently converging results in the future, the streamline distance calculation should be improved to second-order accurate.

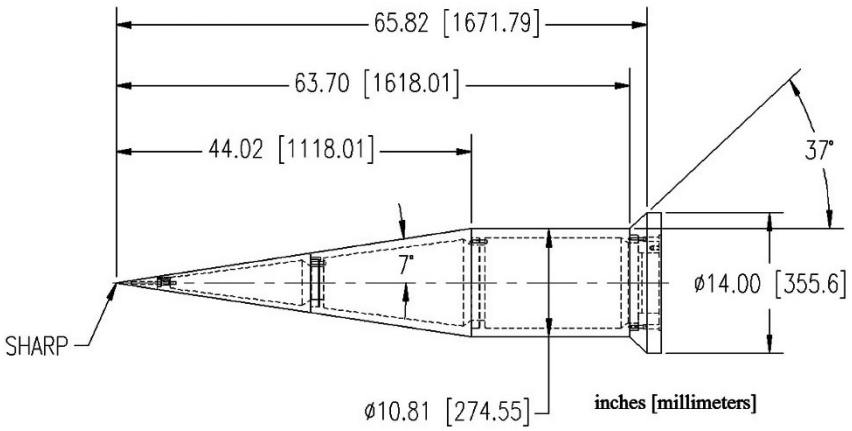

Figure 3-3. The HIFiRE-1 wind tunnel test geometry that shows the fore-cone on the left, the cylindrical section in the center, and the flare on the right, from [1]. The text states that the final nosetip was changed from sharp to a radius of 2.5 mm and the flare angle was changed from 37° to 33°.

3.2.1. MNA+FPBL with 0° Angle of Attack

The MNA+FPBL model with 0° angle of attack case has the option of two different viscous models: flat-plate laminar and flat-plate turbulent using the van Driest model, shown in Figures 3-4 and 3-5. Note that the HIFiRE-1 geometry is shown as a shaded figure in the background of each plot to show the increase in uncertainty due to changes in geometry.

For pressure, both the GCI and order of accuracy perform quite well for the laminar and van Driest cases, except near the discontinuity at the front of the nose cone, which is to be expected. We note that there is a drop in order of accuracy when the angle of the HIFiRE-1 geometry is zero, in the cylindrical portion, since the model is designed to be insensitive when the angle is 0°. For heat flux, the results are less desirable because of the larger sensitivity to the mesh and due to the large variation in order of accuracy, although the numerical uncertainty is still quite small (approximately 3% maximum difference) and the uncertainty and spike in order of accuracy are quite localized. Refinement of the mesh in areas where the angle of the geometry changes should help reduce the increase in numerical uncertainty.

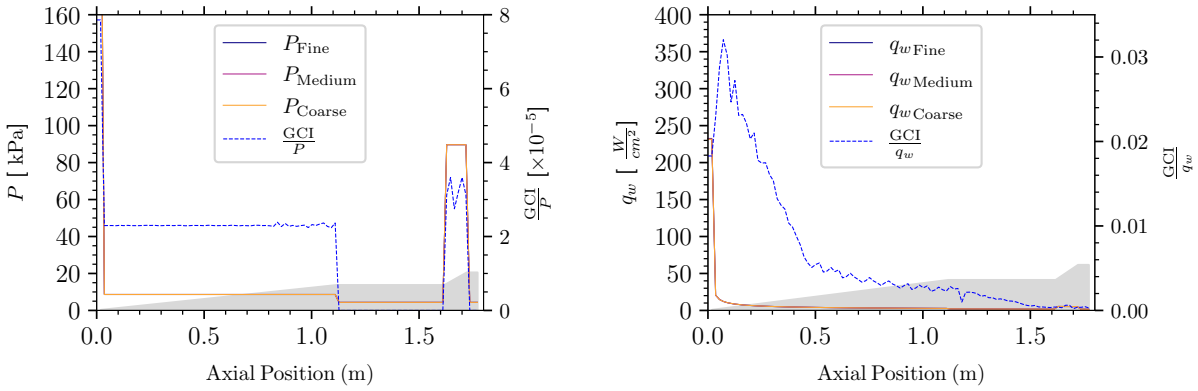

(a) Pressure

(b) Heat flux

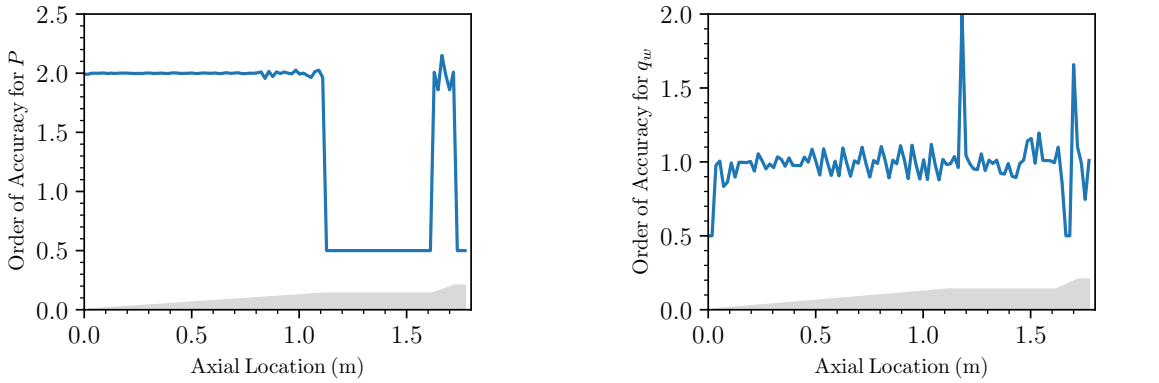

(c) Order of accuracy for pressure

(d) Order of accuracy for heat flux

Figure 3-4. GCI calculation for laminar case with 0° angle of attack.

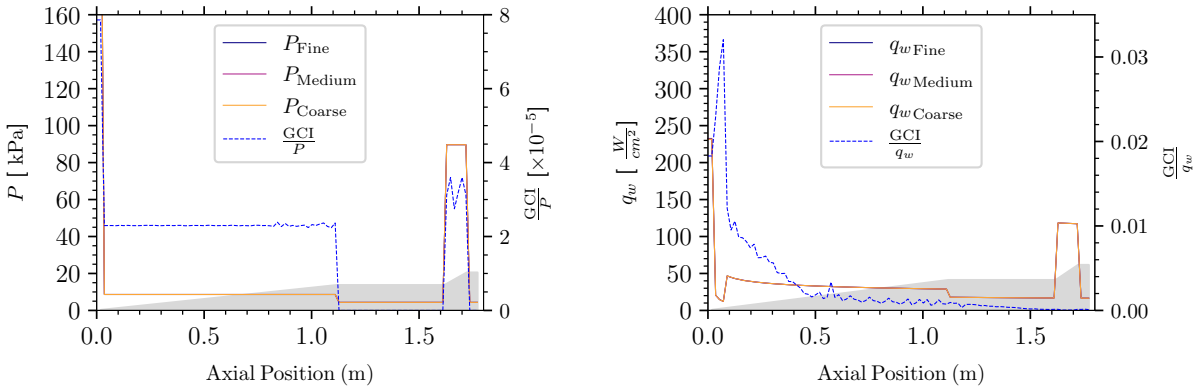

(a) Pressure

(b) Heat flux

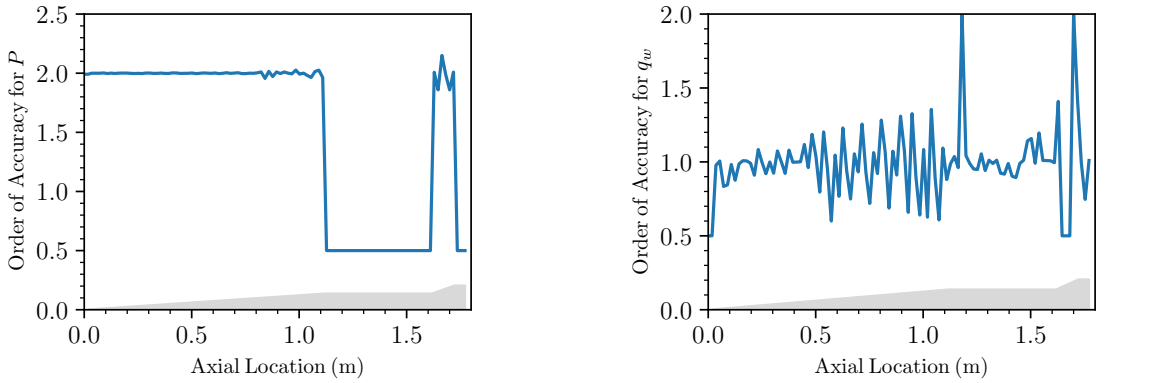

(c) Order of accuracy for pressure

(d) Order of accuracy for heat flux

Figure 3-5. GCI calculation for turbulent (Van Driest) case with 0° angle of attack.

3.2.2. *Euler+MEIT with 0° Angle of Attack*

The Euler+MEIT model with the 0° angle of attack case is shown in Figure 3-6. This case represents the standard mid-fidelity option within MFTK. Note that the HIFiRE-1 geometry is shown as a shaded figure in the background of each plot to show the increase in uncertainty due to changes in geometry.

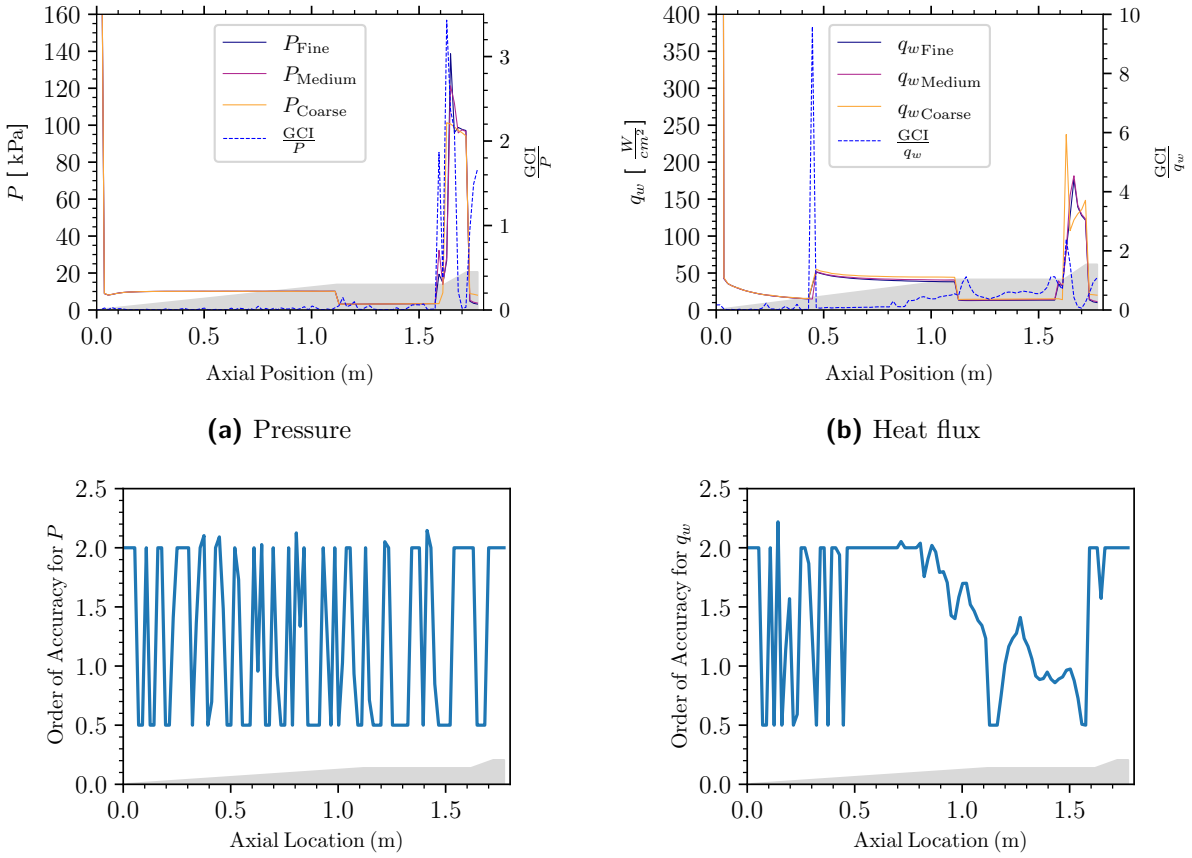

(a) Pressure

(b) Heat flux

(c) Order of accuracy for pressure

(d) Order of accuracy for heat flux

Figure 3-6. GCI calculation for turbulent (MEIT) case with 0° angle of attack.

For pressure, there are areas in the domain that are not fully resolved with a GCI ratio of up to 3.5. Additionally, the order of accuracy confirms this lack of convergence with spikes from the order of accuracy. For heat flux, rather than modeling the laminar-to-turbulent transition region, MFTK currently switches from laminar to turbulent at $x = 0.45$ m. This is a relatively new addition to MFTK to include both laminar and turbulent solutions. At $x = 0.45$ m, the GCI ratio is up to 10.0, which indicates the manual method of modeling the transition region could use improvement. To improve the transition modeling, the transition model should be adjusted to include a length scale to the transition region to ensure a resolvable transition model. In addition to the transition region, the sharp aft region looks to be under-resolved. If the numerical uncertainty is too large, this could be addressed in future studies by locally refining this region.

3.2.3. *RANS with 0° Angle of Attack*

The RANS model with 0° angle of attack case has the option of two different viscous models: Spalart–Allmaras (SA) and Shear Stress Transport (SST), shown in Figures 3-7 and 3-8. These cases represent the high-fidelity options within MFTK. Note that the HIFiRE-1 geometry is shown as a shaded figure in the background of each plot to show the increase in uncertainty due to changes in geometry.

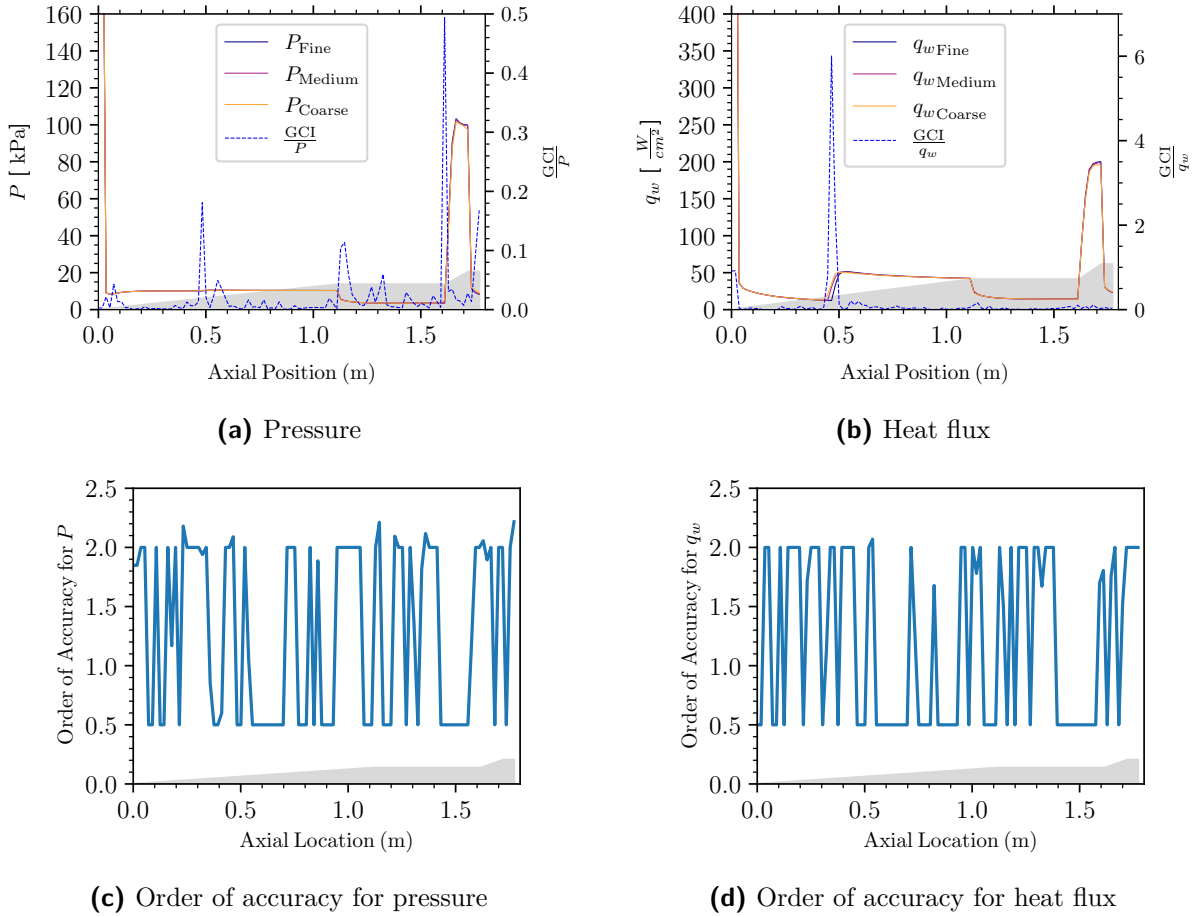

(a) Pressure

(b) Heat flux

(c) Order of accuracy for pressure

(d) Order of accuracy for heat flux

Figure 3-7. GCI calculation for turbulent (SA) case with 0° angle of attack.

For pressure, the GCI and order of accuracy for the SA model performs much better than the SST model, which almost never has an order of accuracy that is close to the theoretical value and a maximum GCI ratio of around 11.0. For heat flux, the results are similar to pressure where the GCI and order of accuracy for the SA model perform much better than the SST model, except for the spike in the GCI ratio near the laminar–turbulent transition region. Regardless of the turbulence model, the chaotic nature of the order of accuracy is concerning and a more refined mesh is probably required unless a large numerical uncertainty is acceptable.

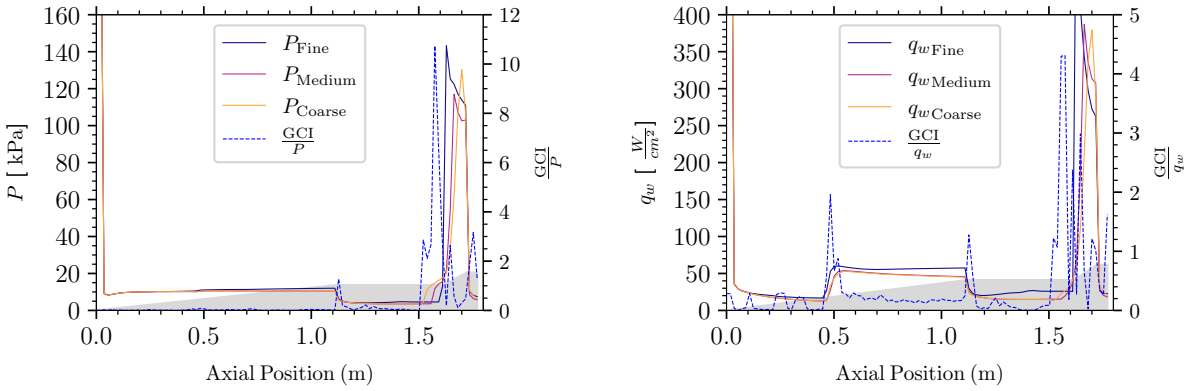

(a) Pressure

(b) Heat flux

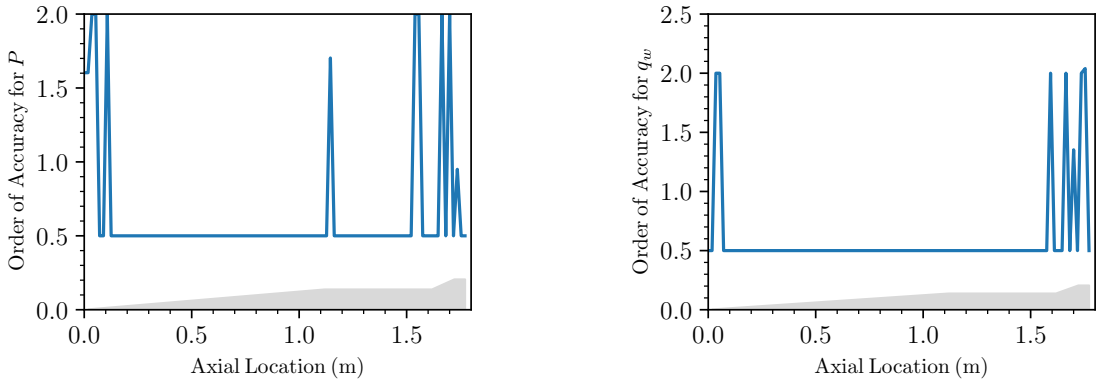

(c) Order of accuracy for pressure

(d) Order of accuracy for heat flux

Figure 3-8. GCI Calculation for turbulent (SST) case with 0° angle of attack.

3.3. Future Work

For future work, additional code verification should be performed for the FPBL, MEIT, and RANS equations to ensure the proper implementation of the models. When reviewing the mid- and high-fidelity numerical uncertainties, the RANS-SA is much lower than the other models. We also point out that even though the RANS-SA model had the lowest numerical uncertainty of the mid- and high-fidelity models, the order of accuracy was sporadic and the GCI value is still quite high. The high GCI value is an important result since these mid- and high-fidelity meshes were considered to be well refined before the analysis was completed. This means that future simulations should use more refined meshes and will unfortunately add to the computational expense, which adds to the appeal of the low-fidelity model. As expected, the low-fidelity MNA+FPBL model's numerical uncertainty is the lowest of all the simulation results. This is due to the simplistic nature of the model and reaching well inside the asymptotic region is less computationally expensive. When these cases are evaluated in the validation chapter of this report, results where the GCI ratio is unacceptably high should either be locally or globally refined to ensure the solution is within the asymptotic region. In addition to local and global mesh refinement, the transition from laminar to turbulent solutions should be improved to ensure the transition is smooth. Without a smooth transition, this region is not able to enter the asymptotic range and will yield large numerical uncertainty.

4. VALIDATION

Validation, or more specifically, model validation, is the process of asking to what degree a model represents physical phenomena for its intended uses [14].

4.1. Model Validation Theory

Though formally defined in the introduction, informally, model validation seeks to determine the degree to which the model is solving the physically appropriate equations. For high-speed aerodynamics, these would include compressible forms of the continuity, momentum, and energy equations. For the turbulent flows, including the full forms of the governing equations (as in Direct Numerical Simulation) is often not tractable; therefore, closure models are frequently used (as in RANS). The inviscid treatment of certain flows is another example of a modeling assumption. Model validation processes can be used to determine the suitability of such modeling assumptions.

Comparing simulation predictions to experimental results is fundamental to model validation. There are several levels of scrutiny in comparisons that are seen in literature. A helpful comparison is found in Figure 12 of [17] that presents six levels of validation comparisons. The first and least descriptive is the viewgraph norm where contours are placed next to each other, but differences in values are often obscured from the wealth of field information and colorful scales. The next plots show several levels of comparisons that switch to a common set of axes that are much better at revealing direct information. Increasing the levels of UQ on measurements and predictions increases the rigor.

The ASME V&V 20 standard goes beyond comparisons in plots to the calculation of validation comparison error and the validation uncertainty [14]. In this standard, the validation comparison error E is defined as

$$E = S - D, \tag{4.1}$$

where S represents the simulation solution and D represents the experimental data. Equation (4.1) provides the simplest validation metric, which nonetheless transitions from the qualitative comparisons in plots to a quantitative measure used to evaluate predictive accuracy. It can be used to reveal trends in model form error over space, time, or parameter sets.

The validation comparison error reveals differences, but how meaningful are those differences, and could experimental and/or modeling uncertainties explain them? To help

answer these questions, ASME V&V 20 also includes the calculation of a validation uncertainty

$$u_{\text{val}} = \sqrt{u_{\text{num}}^2 + u_{\text{input}}^2 + u_D^2}, \tag{4.2}$$

where u_{num} is the numerical uncertainty commonly assessed by grid convergence studies, u_{input} is the input parameter uncertainty propagated through the model, and u_D is the experimental data uncertainty [14]. Equation (4.2) is in the form of a standard uncertainty at the 1σ or 68% confidence level. To calculate the expanded uncertainty at a more typical 2σ or 95% confidence level, the confidence coefficient $C = 2$ can be included as in $U = Cu$ on the uncertainty components or on u_{val}. Throughout this work, uncertainties are presented at the 95% confidence level. The validation uncertainty provides perspective on the validation error. For example, if $|E| \gg u_{\text{val}}$, then model form error is discernible from the relatively small validation uncertainty and model improvements may be prudent if the errors are larger than desired. On the other hand, if $|E| \leq u_{\text{val}}$, model form error is not distinguishable among the validation uncertainty and efforts to reduce uncertainty may be pertinent.

Note that E is the validation comparison error and includes possible errors in measured data and simulation predictions. It is, therefore, not the model form error. The exact model form error is challenging to isolate but can be bounded. In ASME V&V 20 [14], the model form error is bounded by

$$\delta_{\text{model}} \in [E - u_{\text{val}}, E + u_{\text{val}}]. \tag{4.3}$$

This bounding motivates efforts to minimize uncertainty in both experiments and simulations so that the model form error can be known with greater accuracy.

4.2. HIFiRE-1 Wind Tunnel Tests

Experimental data are critical to validation studies, but there are few presented in the public literature for hypersonic aerodynamic vehicles, possibly due to the challenges of measurements under these extreme conditions or the sensitivities of the applications. There are a handful of tests that include a mix of flight and ground tests. These two types have benefits and drawbacks. Flights tests are closer to the intended uses of MFTK, but measurement quantity and quality for aero-only quantities are challenging. Most flight tests of hypersonic vehicles require a thermal protection system that complicates the direct measurement of aerodynamic quantities such as surface pressure, temperature, and heat flux. Also, flight test conditions are only loosely controlled and measured. Conversely, ground tests are farther from the intended uses of MFTK but enable greater instrumentation and control of conditions. Many ground test facilities are shock tunnels that induce hypersonic conditions for a fraction of a second, eliminating the need for thermal protection systems.

Many potential validation data sources were surveyed for this work. One source of hypersonic aerodynamic validation data is the Hypersonic International Flight Research and Experimentation (HIFiRE) program that sought to develop hypersonic technologies. The program included atmospheric flight tests and ground tests in the shock tunnel facilities at the Calspan–University at Buffalo Research Center (CUBRC). Their Large Energy National Shock (LENS) facilities include LENS I, LENS II, and LENS XX [18]. Of particular interest are the HIFiRE-1 wind tunnel tests that have been used for validation data in a number of subsequent publications that were conducted in the LENS I shock tunnel [1].

The HIFiRE-1 wind tunnel tests were selected for a validation application due to hypersonic flow conditions, challenging flow characteristics, turbulence, testing with air, and a wealth of high-quality data that spans a range of angles of attack and Reynolds numbers [1]. One down-side is the low enthalpy conditions in the flow that will not exercise the reacting gas models in the MFTK RANS implementation. The HIFiRE-1 flight test was not selected due to the coning motion during reentry that makes it less ideal for validation [19].

The HIFiRE-1 wind tunnel geometry is shown in Figure 3-3. It has a complex shape with a slender 7° half-angle fore-cone, a cylindrical section in the center, then a blunt flare at the rear. Depending on the run configuration, turbulent transition occurs naturally or is tripped on the fore-cone. The flare causes a separation bubble in the cylindrical section that is a challenge for many RANS models [18]. The test series had a total of over 50 runs in two phases and the model contains a total of almost 100 heat flux sensors and 56 pressure sensors that are located at four different meridional angles.

To provide a sense of the flow field, the Mach number predictions in a two-dimensional, axisymmetric, wall-normal plane for two RANS models are shown in Figure 4-1. The flow is left to right. The solid wind tunnel model is the white region in the lower right and includes the cone, the cylinder, and the flare. The white region in the upper left is not simulated. The RANS Spalart–Allmaras (SA) and RANS Shear Stress Transport (SST) models predict similar flow fields with the exception of the separated region near the cylinder-flare intersection that is more pronounced for RANS-SST.

4.3. Validation Results

The validation studies herein include surface pressure and heat flux comparisons for Run 30, a 0° angle-of-attack case at a relatively high Reynolds number. In addition to traditional comparison plots, the validation comparison error E from (4.1) and validation uncertainty u_{val} from (4.2) are calculated and plotted to enable quantitative comparisons of predictive accuracy at all three fidelity levels of MFTK. The experimental data have known uncertainties [1]. Similarly, the solution-verification studies in Chapter 3 provide numerical uncertainty values u_{num}. Note that for all of the simulation results herein, the medium mesh was used and iterative convergence was achieved by driving normalized residuals

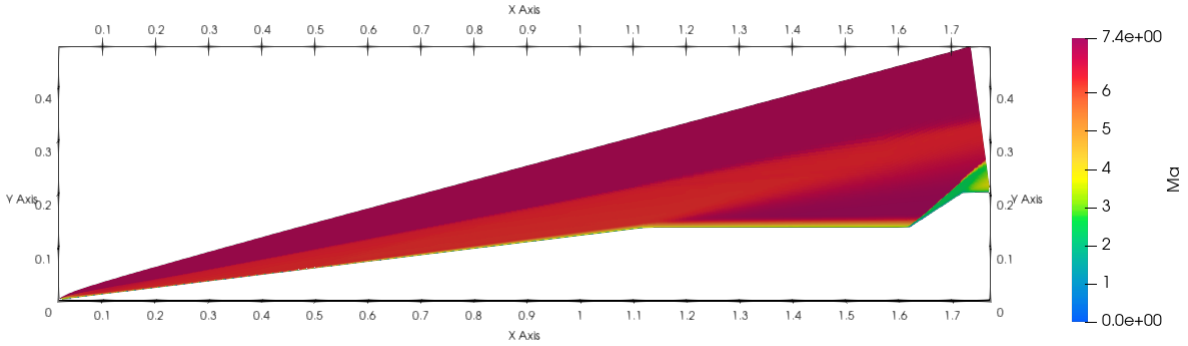

(a) RANS-SA

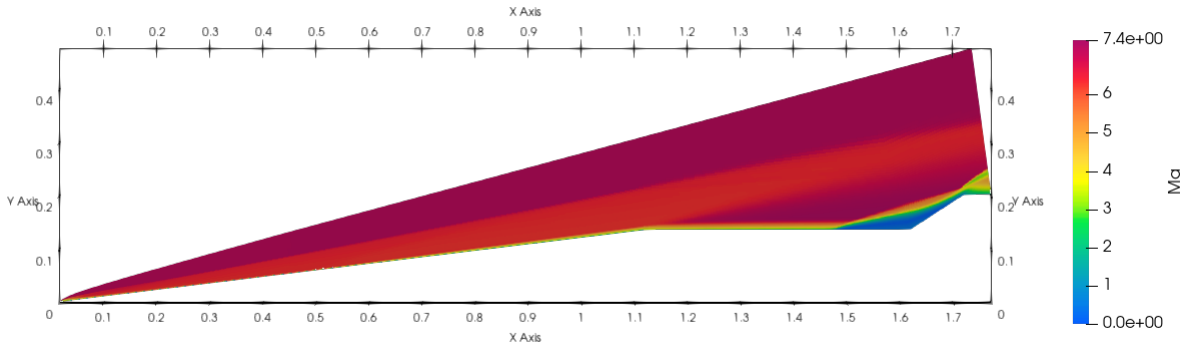

(b) RANS-SST

Figure 4-1. HIFiRE-1 wind tunnel simulation Mach number predictions for RANS-SA and RANS-SST models.

below 10^{-12}. The parameter uncertainty u_{input} is not calculated in this work but recommended for future work.

4.3.1. Surface Pressure Comparisons

The first validation comparison is the surface pressure along the axial length of the vehicle as shown in Figure 4-2. The test vehicle geometry is shown with the second y axis as a gray region to provide background to the drastically different behavior along the length. The results include measured data and predictions from the RANS-SA model, the RANS-SST model, the Euler model combined with the Momentum/Energy Integral Technique (MEIT), and the modified Newtonian aerodynamics (MNA) model combined with flat-plate boundary layer (FPBL) correlations. The experimental pressure uncertainty is 3% [1], interpreted as 3% of reading in the associated error bars/uncertainty bands. The simulations have numerical uncertainty from the GCI results from solution verification shown as shaded regions that are colored according to their respective model color. The data are taken from the 0° meridian that has the most sensors. The fore-cone has very few pressure sensors, but the pressure is nearly constant in this region. The instrumentation density increases towards the rear of the vehicle where the flow is more complex. The pressures increase drastically on the 33° flare region. The predictions used meshes that were derived from the same source. From a 3D source mesh, a 2D axisymmetric mesh with 131,072 cells was derived for the RANS and Euler+MEIT simulations. For the MNA model, which only requires a surface mesh, the 3D surface was extracted from the source mesh.

This figure features an inset plot that highlights the aft end of the cylindrical and the flare regions where the pressure measurements and predictions are quite complex. The RANS predictions compare very well on the fore-cone and cylinder sections, as expected due to the inviscid nature of the surface pressure. However, the agreement breaks down at the separation point leading to the flare, which highlights the known inability of RANS models to capture the complex physics of turbulent flow through a shock/boundary layer interaction [20]. The SA model generally predicts pressure more accurately in this region, though it appears to miss the physics of separation. The SST model over-predicts the separation region, consistent with the findings of modelers associated with the HIFiRE study [18]. The RANS-SA model has low numerical uncertainty while the RANS-SST model has a very large uncertainty as the pressure predictions change drastically in the separation and flare regions.

While others at Sandia National Laboratories have recently completed validation studies with RANS in a similar manner [20], the mid-fidelity Euler+MEIT and low-fidelity MNA+FPBL models have undergone no known validation work. Similar to the two RANS models, the Euler+MEIT predictions are also qualitatively very good in the fore-cone and cylinder sections. The pressure predictions more closely align with those from the SA model in the separation region, though with some noise along the axis. Interestingly, it appears that this mid-fidelity model combination is more accurate than the SST model near this separation. However, the mid-fidelity model is not mesh-converged as evidenced

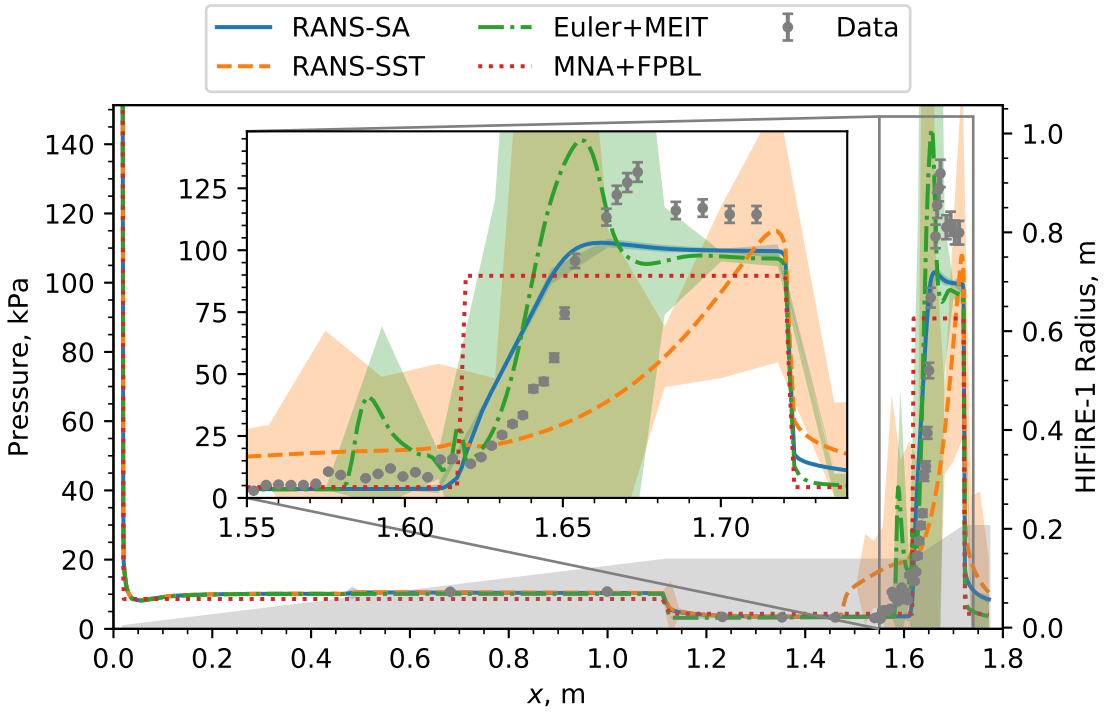

Figure 4-2. HIFiRE-1 wind tunnel test pressure data and predictions.

by the large numerical uncertainty. Quantitative comparisons follow herein that present greater detail.

The surface pressure predictions of the MNA+FPBL are also of high interest. Because MNA is one of the class of so-called 'panel' methods, the only means by which it computes the surface pressure is by using analytic formulas to process the flow through a shock wave and then deflect the flow at the angle of the panel on the surface. These two steps dictate the surface pressure on any forward-facing panel in the solver. The theoretical concept of panel methods, flow deflection without losses or viscous modification, is reasonably true in the limit of infinite Mach and Reynolds numbers and thus is only an approximation at finite values. With this in mind, the MNA solver does a reasonable job predicting the surface pressure on the fore-cone and cylindrical portions of the vehicle. The MNA solver does not model any shock waves or boundary layers and is incapable of predicting the separation point observed in the experiments. The flare portion of the vehicle presents a higher degree of deflection compared to the rest of the vehicle and therefore shows the highest surface pressure, aside from the stagnation point on the nose. The MNA+FPBL models predict the increase in surface pressure at the flare with reasonable accuracy, but do not capture the non-uniform behavior observed in the experiment. The numerical uncertainty is negligible because this model is a panel method for which the pressure predictions are only a function of inflow and the angle between the panel and the flow.

To determine quantitative accuracy, the errors in surface pressure predictions were calculated using (4.1) and normalized by the experimental data for the four models along

the vehicle axis and shown in Figure 4-3. The error is very low in the fore-cone and cylindrical sections as expected with the MNA+FPBL models showing the largest error. The error increases greatly in the separation and flare region with strong positive and negative errors. The validation uncertainty calculated from (4.2), with $u_{\text{input}} = 0$, is also shown as a shaded band to help determine if the validation error is discernible among the uncertainty, which it clearly is for the RANS-SA and MNA+FPBL models but not consistently for others.

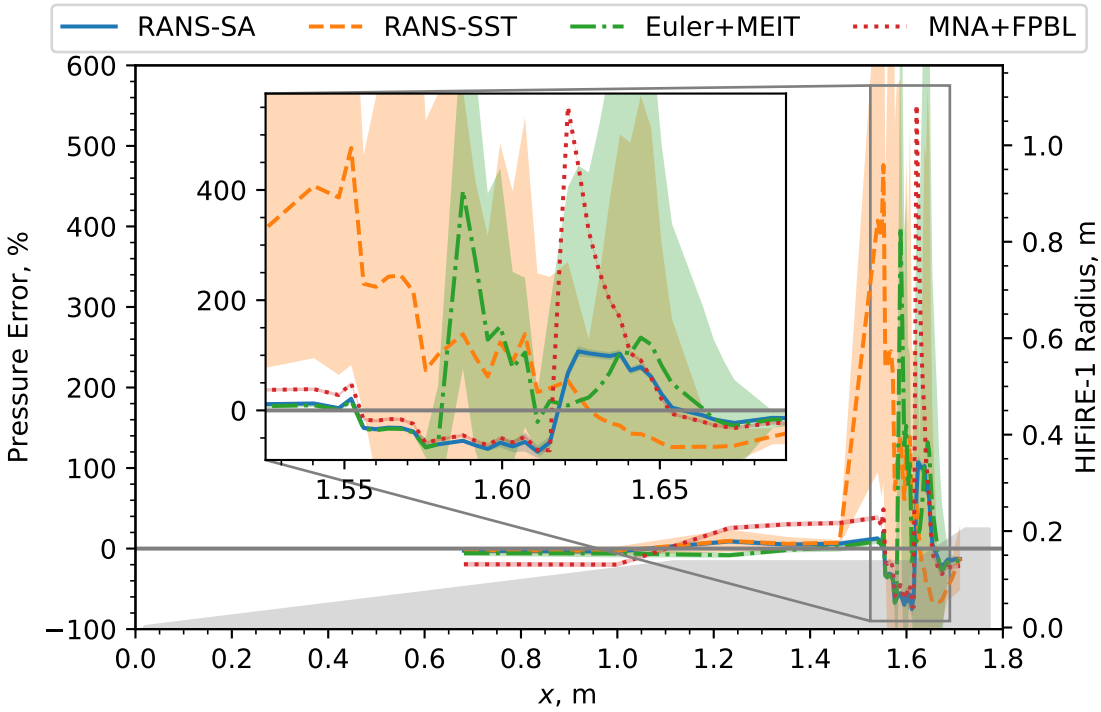

Figure 4-3. HIFiRE-1 pressure prediction error with uncertainty.

Because the validation error along the axis is very noisy with large differences in magnitude in different sections, overall conclusions may be challenging to formulate. To compensate for this, the validation error relative to the experimental data was integrated across all experimental data points for each model independently using a trapezoidal method and plotted in a bar plot in Fig. 4-4. Figure 4-4a only includes the experimental uncertainty of 3%, whereas Fig. 4-4b includes both experimental and numerical uncertainty sources. The accuracy is better shown in Fig. 4-4a. Here, the improved accuracy of the SA model is shown with the subsequent models being Euler+MEIT, MNA+FPBL, and finally SST. The surprisingly high error of SST is due to the over-prediction of the separation region size where the data are relatively low. Again, the validation uncertainty is shown but in the form of uncertainty bands/error bars. If the experimental uncertainty were the only source, the errors would be distinguishable among the uncertainty calculated. However, as Fig. 4-4b shows, the validation uncertainty dominates for the RANS-SST and Euler+MEIT models, such that the error is not discernible. However, it is still distinguishable for the other two models.

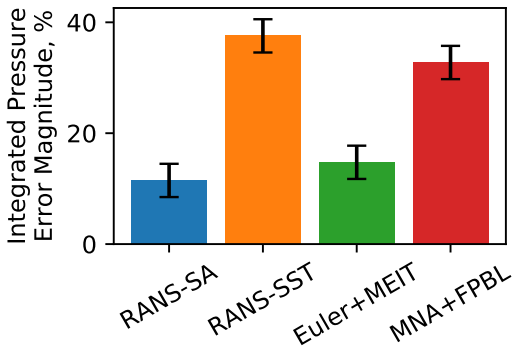

(a) Validation uncertainty only considering experimental source.

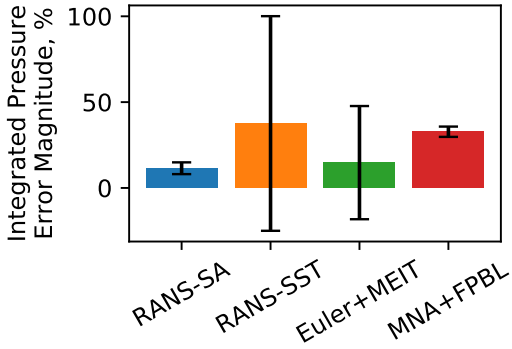

(b) Validation uncertainty considering experimental and numerical sources.

Figure 4-4. HIFiRE-1 pressure prediction error magnitude integrated over data with uncertainty.

The HIFiRE-1 geometry has several different sections that cause the flow to have different behavior, allowing us to evaluate the prediction error in multiple scenarios from the same data set. The pressure error is therefore integrated over sections of a cone with laminar and turbulent portions, a turbulent cylinder, and a turbulent flare with flow separation. The prediction error relative to experimental data is shown for these sections for all four model combinations in Fig. 4-5, except that there are no pressure measurements in the laminar section. Figure 4-5a provides a better look at prediction error by only considering the experimental uncertainty in the validation uncertainty. A more complete understanding is obtained from Fig. 4-5b where the validation uncertainty includes both experimental and numerical sources.

The pressure predictions are much more accurate in the turbulent cone section than the cylindrical or flare sections, suggesting that the flow separation is, in general, more challenging to model. In the turbulent cone section, the higher-fidelity models tend to provide the lowest errors. In the cylindrical section, the RANS-SA and Euler+MEIT model combinations have the most accurate pressure predictions. The RANS-SST model over-predicts the pressure in the separation region where the experimental data are relatively low. In the flare section, the three higher-fidelity models are the most accurate.

4.3.2. Surface Heat Flux Comparisons

The heat flux comparisons are shown in Figure 4-6. Compared with pressure, there are many more sensors and there is an obvious transition from laminar to turbulent flow around $x = 0.45$ m. The experimental heat flux uncertainty is 5% [1]. The numerical uncertainty from solution verification is shown for each model as a shaded band. The RANS solutions do well in capturing both the laminar and turbulent heating on the fore-cone and cylinder. The transition between the boundary layer flow types is enacted by turning on the turbulence production terms at the approximate transition point on the fore-cone. The result of this method is to affect the change of laminar-to-turbulent transition heat flux over a much shorter duration than observed in the experiment. Additionally, the overshoot observed in the data is also missed by the simple transition method. As discussed previously, the separation point location is early in the RANS solution; however, the peak heat flux is consistent with the experimental data. The approach of manually setting the transition location was taken so that the focus is on the predictive accuracy of the physics models, not on the accuracy of a model to predict the transition location, an area that merits further research outside the scope of this work. The numerical uncertainty for the RANS-SA model is generally small throughout, except near the laminar-to-turbulent transition location. Conversely, this uncertainty for the RANS-SST model can be quite large, especially in the turbulent cone section, the aft end of the cylinder, and the flare (of which the latter two are in the predicted separation region).

The Euler+MEIT model combination predictions are very reasonable considering their medium-physics fidelity. The predictive accuracy is nearly as good as the RANS models in the conical section and nearly identical in the cylinder section (except where the RANS-SST model predicts a larger separation bubble on the aft end). The predictions also

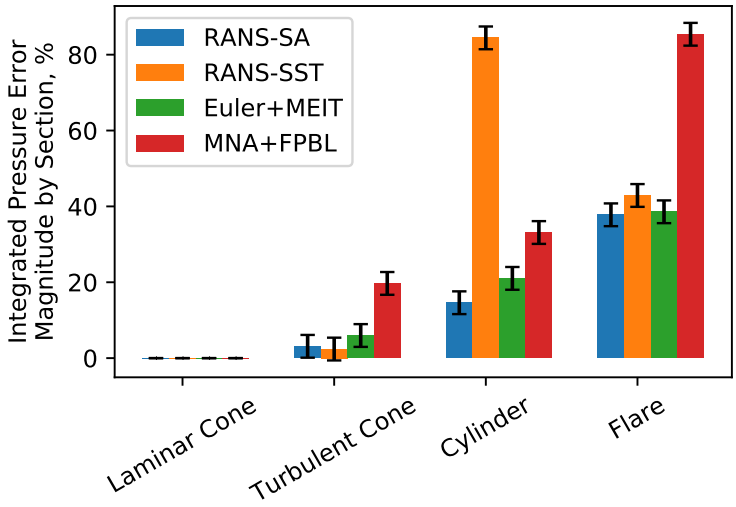

(a) Validation uncertainty only considering experimental source.

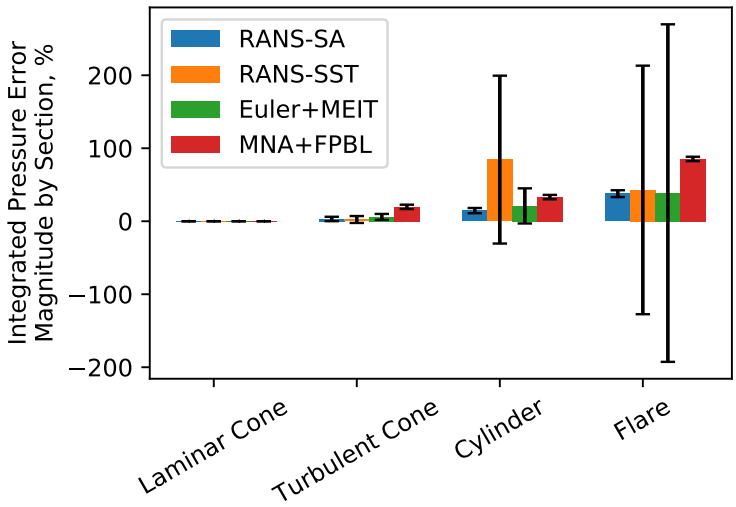

(b) Validation uncertainty considering experimental and numerical sources.

Figure 4-5. HIFiRE-1 pressure prediction error magnitude separated by section with uncertainty.

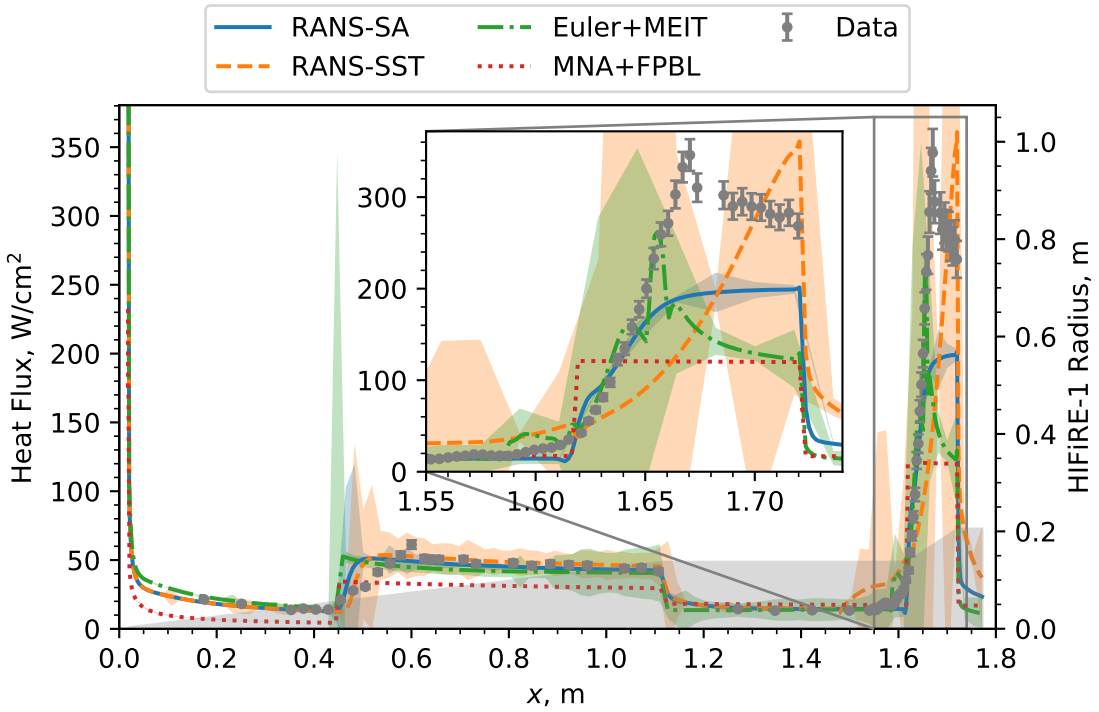

Figure 4-6. HIFiRE-1 wind tunnel test heat flux data and predictions.

match data very well on the fore end of the ramp but decrease too early with an error of about 2×. However, even with this premature decrease, the trend is correct and even better than either RANS model prediction. The numerical uncertainty can be moderately large, especially for $x > 0.9$ m. Note that, as with the RANS models, a laminar version of the model was used upstream of $x = 0.45$ m, and a turbulent version was used downstream.

The MNA+FPBL solver uses a flat-plate boundary layer correlation, a standard laminar correlation, and the Van Driest model for turbulent flow [16] to predict heat flux. As the conical geometry is somewhat removed from a flat plate, it should be expected to have an error of at least $\sqrt{3}$ from the theoretical differences in heat flux. Future implementations of the boundary layer correlations may be targeted toward curvature-aware correlations to reduce this error. However, for the current implementation, the laminar heat flux has an error on the order of 2× from the experiment over the laminar section of the fore-cone. As done with previous models, the laminar and turbulent models were applied fore and aft of $x = 0.45$ m, respectively. Interestingly, the heat flux nearly matches the experiment over the cylinder section of the vehicle, where the flat-plate correlation is very reasonable. On the flare, the error in heat flux is on the order of 3×, which is decent considering the complex fluid dynamics over the flare that are not modeled with the MNA model. Note the nearly flat shape of the heat flux prediction on the ramp where this model does not resolve the complex flow separation. As before, the MNA+FPBL numerical uncertainty is negligible.

As with surface pressure, the heat flux tends to have a lot of variation that can obscure quantitative accuracy conclusions. Therefore, the prediction error with validation

uncertainty clouds for all four model combinations is shown in Figure 4-7. Experimental data are available farther upstream than for pressure, into the laminar cone section of the domain. Accurate predictions in this laminar region are made by all but the MNA+FPBL model which under-predicts the heat flux. In the laminar-to-turbulent transition region, the prediction errors trend from positive to negative and tend to remain slightly negative in the turbulent cone section. In the cylinder section, all models show a high degree of accuracy. Similar to pressure, the errors tend to be largest in the flare region. The uncertainty cloud includes both the experimental and numerical uncertainty from (4.2), of which the latter dominates. Similar to pressure, the validation uncertainty is largest for the RANS-SST and Euler+MEIT models. Here, the turbulent transition region has higher uncertainty, possibly due to the changing cell location where transition is manually set.

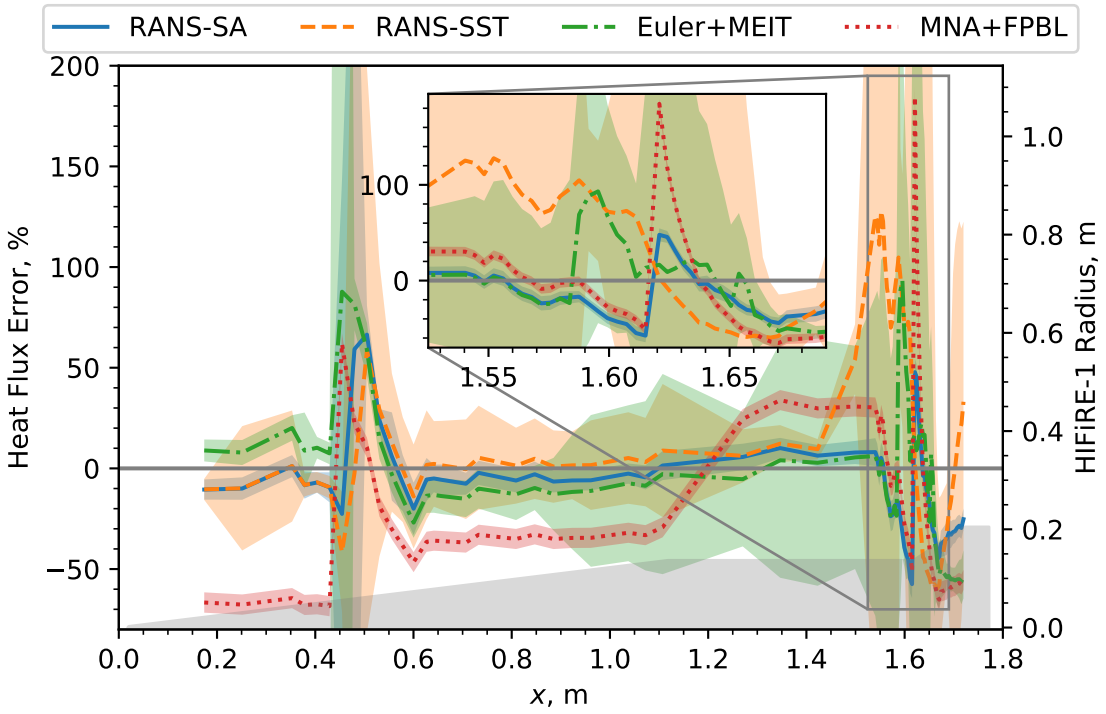

Figure 4-7. HIFiRE-1 heat flux prediction error with uncertainty.

Similar to before, the heat flux prediction errors are integrated to provide a better comparison between accuracy of the different models with the results shown in Fig. 4-8. Figure 4-8a shows the validation error with the uncertainty only considering the experimental source to better highlight the errors. However, Fig. 4-8b includes both experimental and numerical uncertainty sources to provide a more complete representation of the relative sizes of the error and uncertainty. Similar to pressure, the RANS-SA and Euler+MEIT models have the smallest errors. However, the RANS-SST heat flux error is much smaller than with pressure while the MNA+FPBL model has the largest with a difference of about 2×, an expected result. With the more comprehensive validation uncertainty in Fig. 4-8b, this uncertainty overwhelms the prediction error for the

RANS-SST and Euler+MEIT models, suggesting that these models are not mesh-converged.

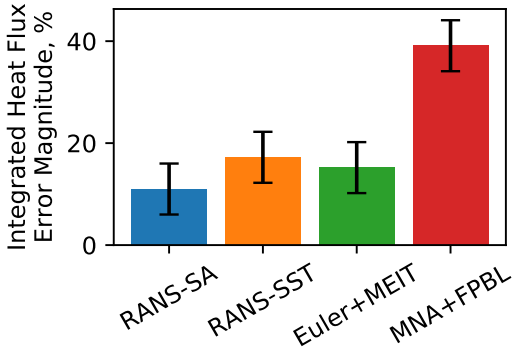

(a) Validation uncertainty only considering experimental source.

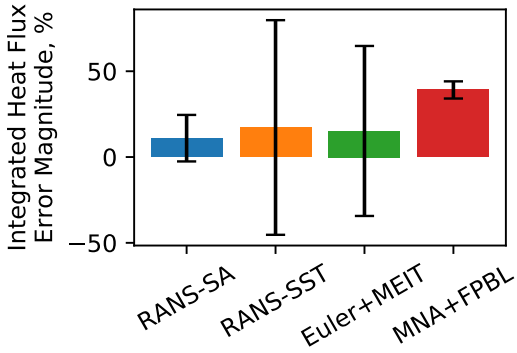

(b) Validation uncertainty considering experimental and numerical sources.

Figure 4-8. HIFiRE-1 heat flux prediction error magnitude integrated over data with uncertainty.

The prediction errors are again separated into different sections in Fig. 4-9 with only the experimental uncertainty considered in Fig. 4-9a to help resolve errors and the more comprehensive uncertainty treatment in Fig. 4-9b. On both the laminar and turbulent sections of the cone, the RANS models are most accurate, followed by Euler+MEIT, with MNA+FPBL least accurate as expected. These three higher-fidelity models have slightly higher error in the turbulent cone section than laminar, an expected result from the higher heat flux and modeling challenges inherent with turbulence modeling. In the cylindrical section, the RANS-SST model has the highest prediction error, likely due to the premature separation prediction. As with the cone, the three higher-fidelity models are most accurate in the flare region. When considering both uncertainty terms available in this work, the uncertainty is consistently larger than the error for the RANS-SST and Euler+MEIT models. Further mesh refinement or potentially mesh quality improvements could reduce the numerical uncertainty and help resolve the predictive accuracy.

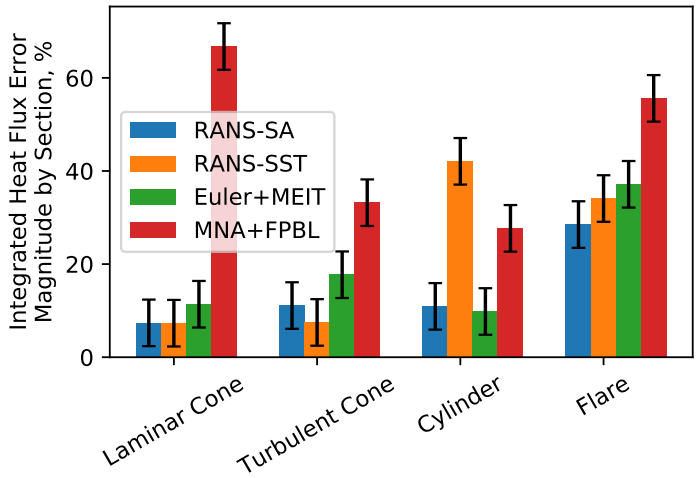

(a) Validation uncertainty only considering experimental source.

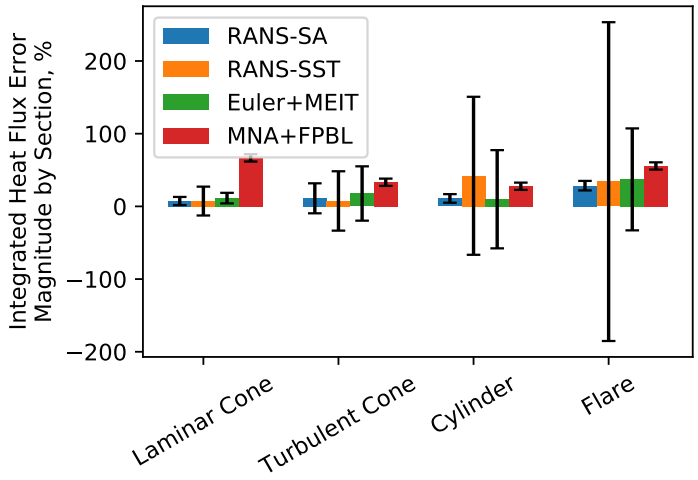

(b) Validation uncertainty considering experimental and numerical sources.

Figure 4-9. HIFiRE-1 heat flux prediction error magnitude by section with uncertainty.

4.3.3. Future Work

This validation study has included a detailed analysis of a single run of the HIFiRE-1 wind tunnel test data set at 0° angle of attack. It will be extended to include cases with nonzero angles of attack and potentially to those at different Reynolds numbers so the predictive accuracy can be quantified under other conditions of interest. Furthermore, other data sets with higher enthalpy flow will be explored to exercise reacting gas models not currently tested with this case. The large magnitude of the numerical uncertainty for the RANS-SST and Euler+MEIT models in the area of separated flow dominates the validation error and should be reduced for more conclusive results. This could be done relatively easily by further mesh refinement. Furthermore, a parameter UQ study could provide added fidelity to the validation uncertainty to help discern validation error from uncertainty.

5. CONCLUSIONS

This work undertakes the first known verification and validation activities for the Multi-Fidelity Toolkit to provide credibility evidence for its use in high-consequence decision making in hypersonic vehicle analysis at a variety of physics-fidelity and computational-expense levels. It has leveraged best practices in both verification and validation. The code-verification activities focused on the modified Newtonian aerodynamics model that is a large component of the low-fidelity capability of MFTK. The other component, the flat-plate boundary layer models, should be the subject of future code-verification efforts. Solution-verification and validation activities were applied to all three fidelity levels of MFTK.

Code and solution verification are vital precursors for high-quality validation activities. By minimizing the coding errors and measuring the numerical uncertainty, we can ensure the impact of discretizing the equations and geometry is minimized. The MNA code-verification results showed that for all QoIs, the difference between the MFTK results and the analytical solution are less than 10^{-13} when the mesh perfectly represents the geometry and the mesh lines up with the streamlines. This means the MNA model has been implemented correctly in MFTK without coding errors for all situations matching the code-verification case scenarios. Additionally, the MNA model has significantly less numerical uncertainty than the Euler+MEIT or either RANS models, which is expected since the asymptotic range for the low fidelity MNA model starts significantly earlier than the Euler+MEIT or either RANS cases. Future Euler+MEIT and RANS-SST cases should be refined where significant numerical uncertainty exists.

This work includes a practical description of model validation theory, an overview of the HIFiRE-1 wind tunnel tests, and validation studies of all three fidelity levels of the MFTK at 0° angle of attack. The relative accuracy of the RANS-SA and RANS-SST models is superior for both pressure and heat flux on the laminar and turbulent fore-cone sections of the HIFiRE-1 geometry. The RANS-SA accuracy remains high for the cylindrical and flare sections as well, while the RANS-SST accuracy suffers due to an over-prediction of the separation region. The RANS-SA model had consistently high accuracy and low numerical uncertainty. The Euler+MEIT pressure predictions are second best in general with very reasonable accuracy throughout the domain. For heat flux, the accuracy was second best overall but followed the RANS models for conical performance. The MNA+FPBL model was generally least accurate for both pressure and heat flux; however, the RANS-SST model had the poorest performance in the cylinder section.

With these considerations and recognizing that these accuracies do not directly extrapolate to other parameter spaces of interest, including high-enthalpy or higher-Mach flows, the RANS-SA model is recommended for situations where the highest accuracy is desired with

the capability to run more expensive models. The RANS-SST model has accurate predictions for conical flows but is not recommended for separated flows, and has the highest numerical uncertainty in this study. This finding is surprising as the SST model was formulated to perform better than its predecessors in separated flows [21]. The high numerical uncertainty of this model in the separation region deserves further attention. The Euler+MEIT model combination has reasonable accuracy and computational expense but higher than expected numerical uncertainty, an area that deserves further investigation. This mid-fidelity model may be a good fit where the RANS models are too expensive. The iterative stability of the Euler simulations was a challenge with these moderately refined meshes, requiring special attention to the run schedule for complete convergence. The MNA+FPBL models have reasonable accuracy, excellent speed, and negligible numeric uncertainty and may be used where a very high number of simulations is required.

This validation activity has focused on accuracy without regard to performance. Nevertheless, the differences in solution speed were notable. While the MNA+FPBL model is solved on a 3D surface mesh for solver convenience, it could theoretically be solved in 2D for this case. Even with this, the speedup is approximately 2,000$\times$ compared to the RANS-SST model. A more thorough evaluation of the trade-offs between accuracy and speed are recommended for a future work, especially as the faster models enable Monte Carlo uncertainty quantification and design/parameter exploration studies much more readily than the high-fidelity models.

REFERENCES

[1] Wadhams, T., Mundy, E., MacLean, M., and Holden, M., "Ground Test Studies of the HIFiRE-1 Transition Experiment Part 1: Experimental Results," *Journal of Spacecraft and Rockets*, Vol. 45, No. 6, 2008, pp. 1134–1148.

[2] Kim, Y., Lee, S., Yee, K., and Rhee, D. H., "High-to-Low Initial Sample Ratio of Hierarchical Kriging for Film Hole Array Optimization," *Journal of Propulsion and Power*, Vol. 34, No. 1, July 2018, pp. 108–115.

[3] ASME, "V&V 10-2019: Standard for Verification and Validation in Computational Solid Mechanics," Tech. rep., American Society of Mechanical Engineers, 2020.

[4] Roache, P. J., *Fundamentals of Verification and Validation*, Hermosa publishers, 2009.

[5] Oberkampf, W. L. and Roy, C. J., *Verification and Validation in Scientific Computing*, Cambridge University Press, 2010.

[6] Salari, K. and Knupp, P., "Code Verification by the Method of Manufactured Solutions," Sandia Report SAND2000-1444, Sandia National Laboratories, June 2000.

[7] Freno, B. A., Carnes, B. R., and Weirs, V. G., "Code-Verification Techniques for Hypersonic Reacting Flows in Thermochemical Nonequilibrium," *Journal of Computational Physics*, Vol. 425, 2021.

[8] Carnes, B. R., Weirs, V. G., and Smith, T., "Code Verification and Numerical Error Estimation for use in Model Validation of Laminar, Hypersonic Double-Cone Flows," *AIAA Scitech 2019 Forum*, American Institute of Aeronautics and Astronautics, 2019, p. 2175.

[9] Roache, P. J., "Perspective: A Method for Uniform Reporting of Grid Refinement Studies," *Journal of Fluids Engineering*, Vol. 116, No. 3, 1994, pp. 405–413.

[10] Rider, W., Witkowski, W., Kamm, J., and Wildey, T., "Robust Verification Analysis," *Journal of Computational Physics*, Vol. 307, 2016, pp. 146–163.

[11] Radtke, G. A., Martin, N., Moore, C. H., Huang, A., and Cartwright, K. L., "Robust Verification of Stochastic Simulation Codes," *Journal of Computational Physics*, Submitted for Publication.

[12] Eça, L. and Hoekstra, M., "Discretization Uncertainty Estimation Based on a Least-Squares Version of the Grid Convergence Index," *Proceedings of the Second Workshop on CFD Uncertainty Analysis*, Instituto Superior Tecnico, Oct. 2006, pp. 1–27.

[13] AIAA, "Guide for the Verification and Validation of Computational Fluid Dynamics Simulations (AIAA G-077-1998 (2002))," 1998.

[14] ASME, "V&V 20-2009: Standard for Verification and Validation in Computational Fluid Dynamics and Heat Transfer," Tech. rep., American Society of Mechanical Engineers, 2009.

[15] Anderson Jr, J., *Hypersonic and High-Temperature Gas Dynamics*, American Institute of Aeronautics and Astronautics, 2019.

[16] White, F. M. and Corfield, I., *Viscous Fluid Flow*, Vol. 3, McGraw-Hill New York, 2006.

[17] Trucano, T. G., Pilch, M., and Oberkampf, W. L., "General Concepts for Experimental Validation of ASCI Code Applications," Tech. Rep. SAND2002-0341, Sandia National Laboratories, Albuquerque, NM (US), 2002.

[18] MacLean, M., Wadhams, T., Holden, M., and Johnson, H., "Ground Test Studies of the HIFiRE-1 Transition Experiment Part 2: Computational Analysis," *Journal of Spacecraft and Rockets*, Vol. 45, No. 6, 2008, pp. 1149–1164.

[19] Kimmel, R. L., Adamczak, D., Paull, A., Paull, R., Shannon, J., Pietsch, R., Frost, M., and Alesi, H., "HIFiRE-1 Preliminary Aerothermodynamic Measurements," *AIAA paper*, Vol. 3413, 2011, pp. 2011.

[20] Kieweg, S., Carnes, B., Freno, B., Phipps, E., Ridzal, D., Rider, W. J., Smith, T. M., Weirs, V. G., Dinzl, D., Howard, M., Wagnild, R., Fisher, T., Mussoni, E., Arienti, M., and Ray, J., "ASC ATDM FY18 Level 2 Milestone Report: Validation of Hypersonic Turbulence Physics in SPARC (Official Use Only-Export Controlled Information)," Tech. Rep. SAND2018-10261, Sandia National Laboratories, 2018.

[21] Menter, F. R., Kuntz, M., and Langtry, R., "Ten Years of Industrial Experience with the SST Turbulence Model," *Turbulence, Heat and Mass Transfer*, Vol. 4, No. 1, 2003, pp. 625–632.

[22] Lees, L., "Hypersonic Flow," *Journal of Spacecraft and Rockets*, Vol. 40, No. 5, 2003, pp. 400–735.

[23] Wagnild, R. M., Dinzl, D. J., Bopp, M. S., Dement, D. C., Robbins, B. A., Bruner, C. W. S., Grant, M. J., Murray, J., and Harper, J. M., "Development of a Multi-fidelity Toolkit for Rapid Aerothermal Model Development," Sandia Report SAND2019-13632, Sandia National Laboratories, Oct 2019.

[24] Van Driest, E., "Calculation of the Stability of the Laminar Boundary Layer in a Compressible Fluid on a Flat Plate with Heat Transfer," *Journal of the Aeronautical Sciences*, Vol. 19, No. 12, 1952, pp. 801–812.

[25] White, F. M. and Christoph, G. H., "A Simple Theory for the Two-Dimensional Compressible Turbulent Boundary Layer," *Journal of Basic Engineering*, Vol. 94, No. 3, 09 1972, pp. 636–642.

[26] Van Driest, E. R., *The Problem of Aerodynamic Heating*, Institute of the Aeronautical Sciences, 1956.

APPENDIX A. Derivation of Modified Newtonian Aerodynamics

This appendix focuses on the derivation of the MNA model for inviscid flow regions and the three flat plate boundary layer (FPBL) models for the viscous flow regions.

A.1. Assumed Inputs

Before discussing the derivation of the MNA model and the FPBL models, the model inputs should be stated. The following constants are used as inputs into MFTK and will be used as part of the analytic solution. The constant names, notation, and values are listed in Table A-1.

Table A-1. Table of values used in code-verification analysis.

Constant Name	Notation	Value	Units
Gas constant for air	R	287.05	J/kg/K
Ratio of specific heats	γ	1.4	–
Prandtl number	Pr	0.73684	–
Freestream density	ρ_∞	0.066958	kg/m^3
Freestream speed	V_∞	2170.0	m/s
Freestream velocity	$\mathbf{V}_\infty$	Problem Specific	m/s
Freestream temperature	T_∞	226.46	K
Wall temperature	T_w	300	K
Sutherland constant C	C_{visc}	1.458×10^{-6}	–
Sutherland constant S	S_{visc}	110.3	–

A.2. Newtonian Theory

Based on Section 3.2 of [15], Newtonian theory computes the pressure applied by the fluid's momentum in

$$p_e - p_\infty = \rho_\infty V_\infty^2 \sin^2\theta, \tag{A.1}$$

where p_e is the edge pressure, p_∞ is the freestream pressure shown in

$$p_\infty = \rho_\infty R T_\infty, \tag{A.2}$$

ρ_∞ is the freestream density, R is the gas constant for air, T_∞ is the freestream temperature, V_∞ is the freestream speed of the flow, and θ is the local surface angle

relative to the freestream flow direction. The ratio between the static pressure and the dynamic pressure is C_p and is defined as

$$C_p = \frac{p_e - p_\infty}{\frac{1}{2}\rho_\infty V_\infty^2}. \tag{A.3}$$

Substituting Eq. (A.1) into Eq. (A.4) results in

$$C_p = 2\sin^2\theta. \tag{A.4}$$

While it is typical to derive these equations on an angled, one-dimensional plate, θ in Eq. (A.4) is the local angle of the surface. This means that these equations are applicable on two- and three-dimensional surfaces. For complex surfaces, θ is calculated by

$$\theta = \sin^{-1}\left(\frac{\mathbf{V}_\infty}{V_\infty}\cdot\mathbf{n}\right). \tag{A.5}$$

where $\mathbf{V}_\infty$ is the freestream velocity and $\mathbf{n}$ is the element surface unit vector. Another important portion of the domain is the other side of the body (also known as the shadow region). Since the shadow region does not undergo the increase in pressure due to the flow, the pressure in the shadow region is the same as p_∞. To account for the shadow region, when $\theta < 0, C_p = 0$.

A.3. MNA Model

The MNA model [22] is an improved method to compute the edge pressure distribution, p_e, over blunt-nosed bodies [15]. Additionally, we use p_e to compute edge velocities, $\mathbf{V}_e$, and edge temperatures, T_e. MNA assumes the pressure at the stagnation point is equal to the stagnation pressure behind a normal shock wave (p_{O_2}). This exactly computes C_p at the stagnation point, so it is natural to replace the factor of two in Newtonian theory with a new coefficient. This new coefficient, $C_{p_{\max}}$ is used in the MNA model, such that Eq. (A.4) becomes

$$C_p = C_{p_{\max}}\sin^2\theta, \tag{A.6}$$

where

$$C_{p_{\max}} = \frac{p_{O_2} - p_\infty}{\frac{1}{2}\rho_\infty V_\infty^2}. \tag{A.7}$$

Noting that $q = \frac{1}{2}\rho_\infty V_\infty^2 = \frac{\gamma}{2}p_\infty M_\infty^2$ (see [15, pg. 44]), Eq. (A.7) is simplified to

$$C_{p_{\max}} = \frac{2}{\gamma M_\infty^2}\left(\frac{p_{O_2}}{p_\infty} - 1\right), \tag{A.8}$$

where γ is the ratio of specific heats and M_∞ is the freestream Mach number and computed using

$$M_\infty = \frac{V_\infty}{\sqrt{\gamma R T_\infty}} \tag{A.9}$$

Using the Rayleigh pitot tube formula from normal shock-wave theory, the relationship between the total pressure behind the pressure wave compared to the freestream pressure is shown by [15, pg. 65]

$$\frac{p_{O_2}}{p_\infty} = \left(\frac{(\gamma+1)^2 M_\infty^2}{4\gamma M_\infty^2 - 2(\gamma-1)} \right) \tag{A.10}$$

By substituting Eq. (A.8) and Eq. (A.10) into Eq. (A.6), the equation is now a function of the ratio of specific heats for air, γ, and M_∞, which matches Eq. (2.3) in [23]. Now that C_p is derived, we can compute p_e by rearranging the terms in Eq. (A.3) to obtain

$$p_e = \frac{1}{2} C_p \rho_\infty V_\infty^2 + p_\infty \tag{A.11}$$

Now that p_e has been derived, edge velocity, $\mathbf{V}_e$, and edge temperature, T_e, can be derived. $\mathbf{V}_e$ is defined as

$$\mathbf{V}_e = V_e \cdot \mathbf{n}_v \tag{A.12}$$

where the edge velocity unit vector, $\mathbf{n}_v$, is computed using the freestream speed of the flow, freestream velocity, and the surface unit vector given by the surface of the body, $\mathbf{n}_s$, in

$$\mathbf{n}_v = \frac{\mathbf{n}_s \times \left(\frac{\mathbf{V}_\infty}{V_\infty} \right)}{\left| \mathbf{n}_s \times \left(\frac{\mathbf{V}_\infty}{V_\infty} \right) \right|}. \tag{A.13}$$

The edge speed $\mathbf{V}_e$ is computed using the edge Mach number, M_e, (see [15, pg. 79]) and the speed of sound, a in

$$V_e = M_e a, \tag{A.14}$$

where

$$M_e = \sqrt{\frac{2}{\gamma-1} \left(\left(\frac{p_e}{p_{e_{\max}}} \right)^{\frac{1-\gamma}{\gamma}} - 1 \right)}, \tag{A.15}$$

$$a = \sqrt{\gamma R T_e}, \tag{A.16}$$

$$p_{\max} = \frac{1}{2} C_{p_{\max}}, \tag{A.17}$$

and

$$T_e = T_\infty \frac{1 + \frac{1}{2}(\gamma-1) M_\infty^2}{1 + \frac{1}{2}(\gamma-1) M_e^2}. \tag{A.18}$$

A.4. Flat Plate Boundary Layer Model

The flat plate boundary layer (FPBL) model is an empirical correlation that computes C_f based on the properties of the flow. C_f is a non-dimensional number to describe the ratio between shear stress and dynamic pressure of the flow. From C_f, the shear stress, $\boldsymbol{\tau}$, and heat flux, q_w, are computed.

A.4.1. Shear Stress

The shear stress model is based on the C_f calculation of flow along a flat plate. There are three models to compute C_f based on two different flow regimes within MFTK. When the flow is characterized as laminar, C_f is based on the calculation from van Driest [24], which is a modification of the Blasius equation. When the flow is turbulent, the user has the choice of using the law-of-the-wall method developed by White and Christoph [25] or a turbulent version of the flat plate model developed by van Driest [26].

Laminar

Based on Equation 7-41b of [16], the laminar coefficient of friction is

$$C_f = \frac{0.664\sqrt{C^*}}{\sqrt{\mathrm{Re}_{xe}}}, \tag{A.19}$$

where the Champman–Rubesin parameter, C^*, is defined by

$$C^* = \frac{\rho^* \mu^*}{\rho_e \mu_e}, \tag{A.20}$$

where the operator * is the characteristic value and the edge Reynolds number, Re_{xe}, is defined by

$$\mathrm{Re}_{xe} = \frac{\rho_e V_e \ell}{\mu_e}, \tag{A.21}$$

where

$$\rho^* = \frac{T_e \rho_e}{T^*}, \tag{A.22}$$

$$\mu^* = C_{\mathrm{visc}} T^* \frac{\sqrt{T^*}}{T^* + S_{\mathrm{visc}}}, \tag{A.23}$$

$$\ell = \mathrm{Dist}\,(x)\,, \tag{A.24}$$

$$T^* = T_e \left(0.5 + \left(\frac{\gamma - 1}{12}\right)\sqrt{\mathrm{Pr}} M_e^2 + 0.5\frac{T_w}{T_e}\right), \tag{A.25}$$

$$\rho_e = \frac{p_e}{R T_e}, \tag{A.26}$$

$$\mu_e = C_{\mathrm{visc}} T_e \frac{\sqrt{T_e}}{T_e + S_{\mathrm{visc}}}. \tag{A.27}$$

Note that $\mathrm{Dist}\,(x)$ is the streamline distance function, Pr is the Prandtl number, which measures the ratio of momentum diffusivity and thermal diffusivity, and C_{visc} and S_{visc} are the Sutherland model coefficients.

Turbulent (White)

Based on Equation 7-132 of [16],

$$C_{f_e} \approx \frac{0.455}{S^2 \ln^2\left(\frac{0.06}{S}\mathrm{Re}_{xe}\frac{\mu_e}{\mu_w}\sqrt{\frac{T_e}{T_w}}\right)}, \tag{A.28}$$

where

$$S = \frac{\sqrt{\frac{T_{aw}}{T_e}-1}}{\sin^{-1}A + \sin^{-1}B}, \tag{A.29}$$

$$A = \frac{2a^2-b}{\sqrt{b^2+4a^2}}, \tag{A.30}$$

$$B = \frac{b}{\sqrt{b^2+4a^2}}, \tag{A.31}$$

$$a^2 = \frac{\gamma-1}{2}M_e^2\frac{T_e}{T_w}, \tag{A.32}$$

$$b = \frac{T_{aw}}{T_w} - 1, \tag{A.33}$$

and

$$\mu_w = C_{\text{visc}}T_w\frac{\sqrt{T_w}}{T_w + S_{\text{visc}}}. \tag{A.34}$$

Based on Equation 7-35 in [16], the adiabatic wall temperature is

$$T_{aw} = T_e + r\frac{{V_e}^2}{2c_p}, \tag{A.35}$$

where the laminar and turbulent recovery factors are defined as

$$r_{\text{laminar}} = Pr^{\frac{1}{2}} \tag{A.36}$$

and

$$r_{\text{turbulent}} = Pr^{\frac{1}{3}}. \tag{A.37}$$

Noting that Equation 7-26 in [16] shows

$$\frac{{V_e}^2}{c_pT_e} = (\gamma-1)M_e^2, \tag{A.38}$$

which is substituted into Equation (A.35) and results in

$$T_{aw} = T_e\left(1.0 + r\left(\frac{\gamma-1}{2}\right)M_e^2\right), \tag{A.39}$$

Turbulent (van Driest)

Based on Equation 7-119 of [16], C_{f_e} is solved iteratively using a Newton iteration. The function that is minimized is

$$\frac{\sin^{-1} A + \sin^{-1} B}{\sqrt{C_{f_e}\left(\frac{T_{aw}}{T_e} - 1\right)}} \approx 4.15 \log\left(\mathrm{Re}_{xe} C_{f_e} \frac{\mu_e}{\mu_w}\right) + 1.7. \tag{A.40}$$

Shear Stress

Once the C_f is calculated by the shear stress, $\boldsymbol{\tau}$, is defined as

$$\boldsymbol{\tau} = \frac{1}{2} C_f \rho_e \mathbf{V_e} V_e \tag{A.41}$$

Note: for turbulent cases, MFTK assumes $C_f \approx C_{f_e}$ based on Equation 7-39 in [16].

A.4.2. Heat Flux

Using the C_f computed above, the heat flux is computed using the Reynold's analogy. Based on Equation 7-15 in [16], the heat coefficient, C_h, is computed using

$$C_h = \frac{q_w}{\rho_e V_e c_p \left(T_{aw} - T_w\right)} = \frac{C_f}{2\mathrm{Pr}^{2/3}}, \tag{A.42}$$

where

$$c_p = \frac{\gamma R}{\gamma - 1}. \tag{A.43}$$

Note that the Reynold's analogy assumes $\mathrm{Pr} = 1$ and a pressure gradient of zero [16]. In addition, the power of Pr in Equation (A.42) is changed from that in Equation 7-15 in [16] to apply to both laminar and turbulent flows. Rearranging for q_w, Equation (A.42) becomes

$$q_w = \frac{C_f}{2\mathrm{Pr}^{2/3}} \rho_e V_e c_p \left(T_{aw} - T_w\right). \tag{A.44}$$

DISTRIBUTION

Email—Internal [redacted]

Name	Org.	Sandia Email Address
Greg Weirs	1446	vgweirs@sandia.gov
Jeff Payne	1510	jlpayne@sandia.gov
Matthew Barone	1515	mbarone@sandia.gov
Paul Delgado	1515	pmdelga@sandia.gov
Derek Dinzl	1515	djdinzl@sandia.gov
Nathan Miller	1515	nmille1@sandia.gov
Bryan Morreale	1515	bjmorre@sandia.gov
Eric Robertson	1515	edrobe@sandia.gov
Justin Smith	1515	jussmit@sandia.gov
Ross Wagnild	1515	rmwagni@sandia.gov
Walt Witkowski	1540	wrwitko@sandia.gov
Matthew Bopp	1541	msbopp@sandia.gov
Paul Crozier	1541	pscrozi@sandia.gov
Travis Fisher	1541	tcfishe@sandia.gov
Lauren Beghini	1544	llbeghi@sandia.gov
Brian Carnes	1544	bcarnes@sandia.gov
Kevin Dowding	1544	kjdowdi@sandia.gov
Brian Freno	1544	bafreno@sandia.gov
Sarah Kieweg	1544	skieweg@sandia.gov
Jared Kirsch	1544	jkirsch@sandia.gov
Aaron Krueger	1544	amkrueg@sandia.gov
Blake Lance	1544	blance@sandia.gov
Josh Mullins	1544	jmullin@sandia.gov
Bill Rider	1544	wjrider@sandia.gov
Justin Winokur	1544	jgwinok@sandia.gov
Jon Murray	5422	jmurray@sandia.gov
Chisom Wilson	5913	cswilso@sandia.gov

Name	Org.	Sandia Email Address
Leah Tuttle	5914	lworrel@sandia.gov
Alex Stevenson	5915	asteven@sandia.gov
Amanda Dodd	8750	ajbarra@sandia.gov
Technical Library	1911	sanddocs@sandia.gov

Sandia National Laboratories is a multimission laboratory managed and operated by National Technology & Engineering Solutions of Sandia LLC, a wholly owned subsidiary of Honeywell International Inc., for the U.S. Department of Energy's National Nuclear Security Administration under contract DE-NA0003525.